IV. ÖRÆFAJÖKULL VOLCANO: NUMERICAL SIMULATIONS OF ERUPTION-INDUCED JÖKULHLAUPS USING THE SAMOS FLOW MODEL

Ásdís Helgadóttir *, Emmanuel Pagneux *, Matthew J. Roberts *, Esther H. Jensen *, Eiríkur Gíslason *

* *Icelandic Meteorological Office*

1. Introduction

This study identifies regions around Öræfajökull Volcano that would be liable to flooding in the event of a subglacial eruption. Melting scenarios (Gudmundsson *et al.*, 2015) are used to simulate the routing of glacial outburst floods (jökulhlaup) over the ice surface and the propagation of floodwater from the base of the glacier on the western and southern flanks of the volcano. Jökulhlaups are simulated as fluids using the SAMOS numerical model, developed for shallow and fast moving granular gravity currents (Zwinger *et al.*, 2003). The uncertainty in rheology of the floods is dealt with by using predefined Manning's *n* coefficients ranging 0.05–0.15. Simulations are made for outburst floods caused by: (i) a caldera eruption, (ii) flank eruptions, and (iii) pyroclastic density currents.

The main objective of the study is to provide information on inundation extent, maximum depths of flooding, maximum flow speeds, and minimum surface transport times, computed for several scenarios and aggregated into thematic datasets. Aggregated results on inundation extent are used in an assessment of the populations exposed to floods (Pagneux, 2015a) while information on maximum flood depths and maximum flow speeds serve as input for rating flood hazards (Pagneux and Roberts, 2015). Results on minimum surface transport time found in this study are used, along with estimates of eruption onset time, subglacial retention time and subglacial transport time (Gudmundsson *et al.*, 2015), in an assessment of the time available for evacuating the areas at risk of flooding (Pagneux, 2015b).

1.1. Past volcanogenic floods

Since Iceland was first populated in 874 CE, two eruptions have occurred beneath the Öræfajökull ice-capped stratovolcano (Figure IV-1). The first observed historical eruption occurred in mid-June 1362, and the second eruption began on 7 August 1727 (Thorarinsson, 1958). Both eruptions were accompanied by a massive, short-lived jökulhlaup that inundated several areas simultaneously. Accounts of the 1727 eruption reveal that it rose rapidly, within hours, to a maximum discharge that was exceptionally large compared to the volume of floodwater drained. For the 1362 jökulhlaup, Thorarinsson (1958) estimated a maximum discharge of ~100,000 m^3/s, attained within a matter of hours. Debris transport was also a significant factor during both jökulhlaups. Debris-laden flows would have comprised juvenile eruptive material, glacial ice, and glaciofluvial sediments, as described in chapter III (Roberts and Gudmundsson, 2015).

The 1362 jökulhlaup is thought to have burst primarily from the glaciers Virkisjökull, Falljökull, and Kotárjökull (Thorarinsson, 1958). Apparently, the 1727 jökulhlaup from Kotárjökull was comparable in size to the 1362 jökulhlaup from the same glacier (Thorarinsson, 1958). However, the 1362 jökulhlaup from Falljökull was much larger than the 1727 jökulhlaup there. Similar to modern-day volcanogenic floods from steep, ice-capped volcanoes (Tómasson, 1996; Magnússon *et al.*, 2012a; Waythomas *et al.*, 2013), it is probable that the 1362 and 1727 jökulhlaups burst initially through the surface of the ice cap at high elevation. Flood sediments from the 1362 jökulhlaup extend over a much greater area than those from the 1727 jökulhlaups, especially towards the northwest and west of Falljökull (Thorarinsson, 1958). Pyroclastic flows would have been prevalent during eruptions of Öræfajökull. These flows would have scoured large zones of the ice cap, causing significant and pervasive ice-melt.

For a full description of the 1362 and 1727 jökulhlaups, see chapter II (Roberts and Gudmundsson, 2015).

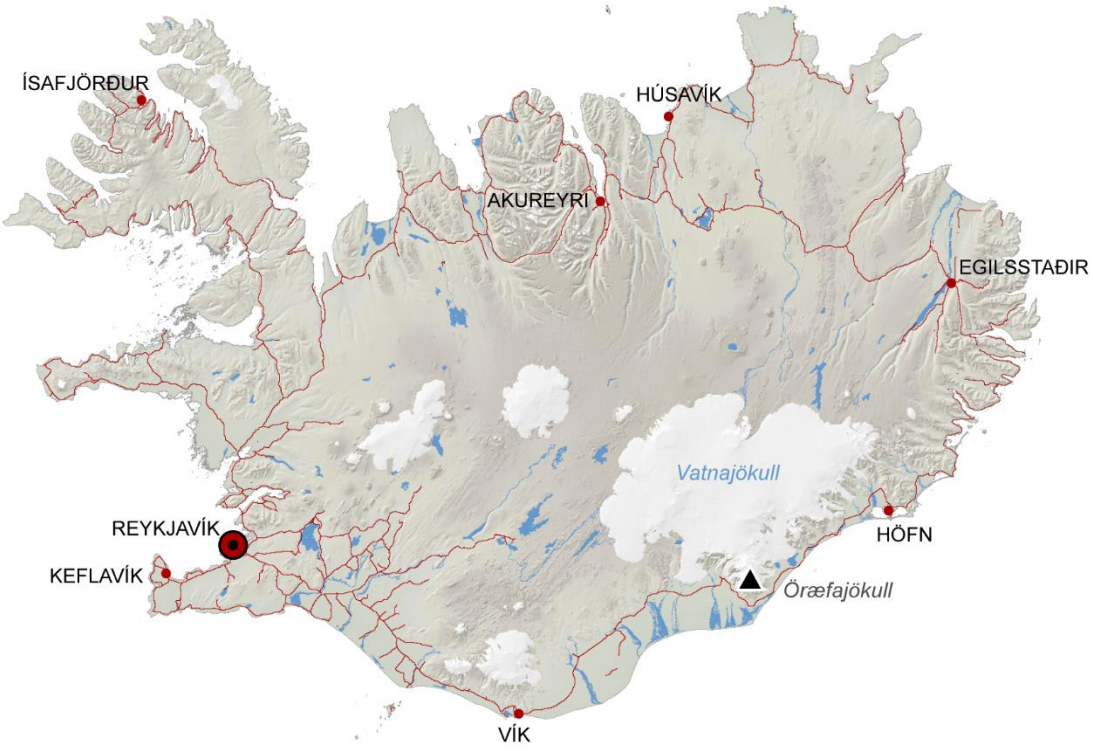

Figure IV-1: Öræfajökull ice-capped stratovolcano, shown by a black triangle, is a separate accumulation area of the Vatnajökull ice cap in south-east Iceland.

1.2. Melting scenarios

Ten melting scenarios relating to volcanic eruptions of various sizes, types, and locations were considered in the modelling of floods due to eruptions of Öræfajökull volcano. Full description of the scenarios is given in chapter III (Gudmundsson *et al.*, 2015).

Flow simulations were restricted to primary jökulhlaups, i.e. floods induced by the eruption itself. A distinction was made between floods due to a caldera eruption, floods due to a flank eruption, and floods due to pyroclastic density currents. Post-eruptive floods, as well as syn-eruptive floods due to precipitation, were not considered in the modelling. Meltwater volume and maximum peak discharge were determined for each scenario using an order-of-magnitude approach (Table IV-1, Figure IV-2). A comparison can be made with the explosive eruptions of Mount Redoubt in 2009, which produced lahars having volumes of 10^7–10^8 m^3 and peak discharges of 10^4–10^5 m^3/s (Waythomas *et al.*, 2013).

Table IV-1: Melting scenarios, with special reference to risk source, meltwater origin and peak discharge (Gudmundsson et al., 2015).

Scenario ID	Glacier catchment	Risk source	Meltwater origin	Peak discharge (m^3/s)
S01c	Virkisjökull – Falljökull (VIR)	Caldera eruption	Falljökull – Virkisjökull	10^5
S01f		Flank eruption	Falljökull – Virkisjökull	10^4
S02c	Suðurhlíðar (SUD)	Caldera eruption	Kotárjökull	10^5
S02f		Flank eruption	Kotárjökull	10^4
S03f		Flank eruption	Stigárjökull	10^4
S03p		Pyroclastic flow	East from Rótarfjallshnúkur*	$3 \cdot 10^4$
S04c	Kvíarjökull (KVI)	Caldera eruption	Kvíarjökull	10^5
S04f		Flank eruption	Kvíarjökull	10^4
S05p	Svínafellsjökull (SVI)	Pyroclastic flow	Svínafellsjökull, south from Svínafellshryggur Ridge	10^4
S06p		Pyroclastic flow	Svínafellsjökull, north from Svínafellshryggur Ridge	10^4

*Kotárjökull excluded

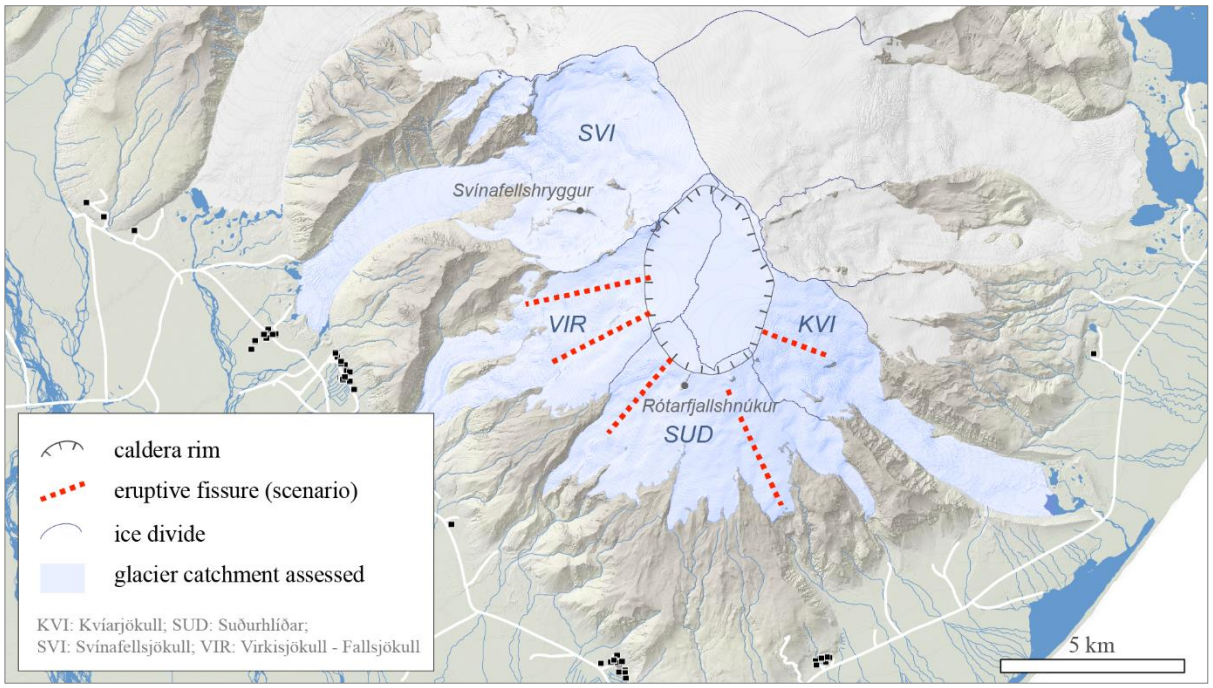

Figure IV-2: Hypothetical eruptive fissures proposed by Gudmundsson et al. (2015). Delineation of the caldera rim is based on ice thickness estimations by Magnússon et al. (2012b). Ice divide is based on airborne LiDAR survey performed in 2011 (see section 3.2.2).

2. Modelling assumptions

Recent observations of high-magnitude jökulhlaups due to volcanism have shown that floodwater often bursts through the surface of steeply sloping glaciers (Roberts, 2005; Magnússon *et al.*, 2012a). This was also the case for large jökulhlaups from the outlet glaciers Kötlujökull (Mýrdalsjökull) and Skeiðarárjökull (Vatnajökull) in 1918 and 1996, respectively (Roberts, 2002). Likewise, anecdotal accounts of the 1727 jökulhlaup from Öræfajökull describe water draining from the glacier. Given that ice thicknesses on the upper slopes of Öræfajökull, outside the volcano's caldera, are widely less than 100 m (Magnússon *et al.*, 2012b), it is likely that floodwater would emerge from crevasses at elevations exceeding 1,000 m AMSL. Hence, for the simulations in this study, floodwater descends initially from the surface of the ice cap at predetermined elevations. In reality a fraction of the flood would also propagate across the glacier bed, but such routing is not considered here. This is in agreement with recent observations of volcanogenic jökulhlaups in Iceland and Alaska (Magnússon *et al.*, 2012a; Waythomas *et al.*, 2013). Significant volumes of snow and ice would be incorporated into a surface-based (supra-glacial) flow. We make no attempt to incorporate the dynamic effects of ice-block transport and floodwater bulking. However, the increased friction resulting from this is taken into account indirectly by using a higher Manning's roughness coefficient (n). The geomorphic consequences of ice-block deposition are addressed by Roberts and Gudmundsson (2015).

3. SAMOS modelling

Several numerical flow models have been used in recent years in the modelling of volcanogenic floods, including LaharZ (e.g. Hubbard *et al.*, 2007; Capra *et al.*, 2008; Muños-Salinas *et al.*, 2009; Magirl *et al.*, 2010; Muños-Salinas *et al.*, 2010), Titan2D (e.g. Charbonnier and Gertisser, 2009; Charbonnier *et al.*, 2013), and VolcFlow (e.g. Charbonnier *et al.*, 2013).

In this study, the SAMOS numerical model is used for the simulation of jökulhlaups. SAMOS is a two dimensional depth-averaged numerical avalanche model initially developed for the Austrian Avalanche and Torrent Research Institute in Innsbruck to model dry-snow avalanches (Sampl *et al.*, 2004; Sampl and Granig, 2009; Zwinger *et al.*, 2003). The model has been used intensively in Iceland in the assessment of run-out zones of snow avalanche (Gíslason and Jóhannesson, 2007), and occasionally in the assessment of floods caused by volcanic eruptions (Hákonardóttir *et al.*, 2005).

3.1. Benefits and constraints

3.1.1. Benefits

Initially developed to model dry-snow avalanches, SAMOS allows the physical properties of the gravity current to be adjusted and fit liquid flow and, therefore, the model is suitable for the modelling of bursts of water on steep slopes. Additionally, SAMOS offers a broad range of model outputs (Table IV-2) that fit with the aim of this study, whose main objective is to provide critical information on flood depths, flow speeds, and flood transport times.

Table IV-2: Comparison of model outputs in LaharZ and SAMOS numerical models.

	LaharZ	**SAMOS**
Inundation extent	✓	✓
Depths of flooding		✓
Flow speeds		✓
Peak pressure		✓
Transport times		✓

3.1.2. Constraints and limitations

Several constraints or limitations inherent in using SAMOS should be named. First, supraglacial floods are simulated as instant release waves and the effects of sediment bulking and de-bulking (erosion and entrainment) are not taken into account. Hydraulic equations at each location are solved using a digital surface model that remains unchanged during simulations. During such sediment-loaded floods, pronounced landscape change is likely to occur (Roberts and Gudmundsson, 2015), thus affecting the evolution of the floodplain during the jökulhlaup, as well as influencing the characteristics of future floods in the region. SAMOS is unable to take such dynamic geomorphic changes into account.

Secondly, floods are simulated in SAMOS as viscous fluids, i.e. as water, and not as hyperconcentrated flows or flows with significant amounts of debris (see Figure IV-3).

Two main courses are generally taken to simulate flows with large amounts of debris (i.e. Non-Newtonian fluids). One is to consider debris flows as a viscous flow with force-free particles (Bagnold, 1954; Takahashi, 1978; Lun *et al.*, 1984; Savage, 1984), which is mathematically simple but leads to unrealistic solutions for water-debris mixtures (Coussot *et al.*, 1996). The other method is to use various viscoplastic flow models like the Bingham (Bingham, 1916; Bingham *et al.*, 1919) or Herschel-Bulkley model (Herschel and Bulkley, 1926). Those viscoplastic flow models are chosen since the particles in debris flow yield stress and the combined fluid shows non-Newtonian characteristics (i.e. viscous stress is not proportional to shear stresses) (Leyrit *et al.*, 2000).

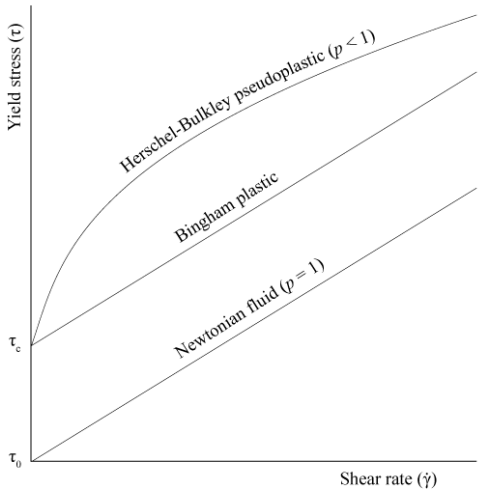

Figure IV-3: Yield stress ($\tau = \tau_c + \dot{\gamma}^p$, where τ_c is the shear stress at zero shear rate and p a positive parameter (Coussot et Meunier, 1996) as a function of share rate ($\dot{\gamma}$) for various fluid models. For Newtonian fluids, yield stress and shear rate are linearly dependent and at zero shear rate the yield stress is zero. Viscoplastic fluids can be modelled with the Bingham model or the Herschel-Bulkley model. For both viscoplastic models at zero shear rate yield stress is not zero. For the Bingham plastic model yield stress and shear rate are linearly dependent but the Herschel-Bulkley model takes shear thinning into account.

In the Bingham model, yield strain and rate of shear strain are linearly dependent but at zero rate of shear strain the yield stress is not zero (see Figure IV-3). In the Herschel-Bulkley model the shear thinning behaviour of water-clay-grain mixtures is taken into account and the magnitude of the shear stress, τ, is given by $\tau = \tau_c + \dot{\gamma}^p$ where τ_c is the shear stress at zero shear rate, $\dot{\gamma}$ is the shear rate and p is a positive parameter (Coussot and Meunier, 1996). The Bingham model has been used for debris flow modelling by Johnson (1970) and Daido (1971) to name a few and the Herschel-Bulkley model has as well been used by multiple researches (Michaels and Bolger, 1962; Nguyen and Boger, 1983; Locat and Demers, 1988; Major and Pierson, 1992; Coussot and Piau, 1994; Wang *et al.*, 1994, Atapattu *et al.*, 1995). For more methods and details on viscoplastic fluids see, for example, the review paper by Coussot and Meunier (1996) and references therein. However, it should be noted that Coussot (1994) has shown that gradually varying mudflows experience the same flow characteristics (hydraulic jump, subcritical and supercritical regimes, instability and more) as water flow and when viscosity parameters are adequately chosen, St.Venant derived equations (as SAMOS is based on) can be used for studying natural flows within small spatial and temporal scales (Coussot and Meunier, 1996).

3.2. Input data and modelling parameters

In this study, the input data required for flood simulation using SAMOS are: (i) physical properties (including roughness parameters); (ii) topographic envelope; (iii) predefined release areas; and (iv) the height of the water column in the release area (i.e. initial flow depth), which in the SAMOS formulation determines the peak discharge.

3.2.1. Rheology

In order to define the rheology for glacial outbursts in SAMOS, the bed friction angle is set to zero and the turbulent friction coefficient is adapted to fit a predefined average Manning's *n* coefficient value. The Manning's *n* coefficient is an empirical coefficient with dimensions $s/m^{1/3}$. It represents flow roughness and ranges from 0.035 to 0.15 (Chow, 1959; Gerhart *et al.*, 1993). The Manning's *n* values used in this study were derived from previous glacial outbursts and roughness estimates for river-beds.

Several factors influence the Manning's *n* value, including surface roughness and sinuosity of channels (Table IV-3). Land-scapes in Iceland are typically devoid of mature trees and other vegetation that would lead to high frictional effects. Although the outwash plains (*sandar*) around Öræfajökull are low-angled and relatively smooth, a volcanogenic jökulhlaup would be laden with friction-adding debris. In addition to coarse-

grained eruptive products, masses of glacial ice would be mobilised by deep, fast-flowing water. Similarly, erosion of unconfined deposits such as glaciofluvial sediments would lead to hyperconcentrated flows, which cannot be modelled adequately using SAMOS.

Table IV-3: Examples of the empirical Manning's n for channels (After Chow, 1959).

Surface	Manning's *n*
Asphalt, smooth	0.013
Excavated channel	0.028
Clean, straight channel full of water	0.03
Streams containing cobbles and large boulders	0.05
Forested area	0.12

Based on accounts of the 1918 eruption of the Katla subglacial volcano, Tómasson (1996) estimated floodplain Manning's *n* coefficients of 0.08 to 0.1. Nye (1976) calculated the Manning's *n* coefficients of the Grímsvötn 1972 jökulhlaup and got 0.12 and when Björnsson (1992) repeated the Manning's *n* coefficient calculations, resulting in an estimate of 0.08. It should be noted that estimations in Nye (1976) and Björnsson (1992) are inferences about the roughness of the subglacial flood-path, not the sub-aerial route.

Russell *et al.* (2010) estimated the Manning's *n* coefficients of 13 cross sections following a jökulhlaup from Sólheimajökull in July 1999. Various methods were used, including measurements based on bulk sediment samples collected in the days after the jökulhlaup. The estimated Manning's *n* coefficients of the cross sections ranged from 0.03 to 0.08. Gíslason (2012) used HEC-RAS to reconstruct the supraglacial jökulhlaup in on the southern slope of Eyjafjallajökull in 2010. There, he concluded the Manning's *n* coefficient on the lower slopes to be 0.03–0.04 whereas in the steep slopes Manning's *n* values of 0.1–0.13 were more realistic. Hákonardóttir *et al.* (2005) used SAMOS to simulate supraglacial outbursts on the southern slopes of Eyjafjallajökull volcano. The uncertainty in rheology of the supraglacial floods was dealt with by choosing three Manning's values $n = 0.05$, $n = 0.10$, $n = 0.15$. In relation to inundation area, the results of Hákonardóttir *et al.* (2005) are in good accordance with the observations made in the Svaðbælisá Valley after the 2010 jökulhlaup in Eyjafjallajökull (Snorrason *et al.*, 2012). Elíasson *et al.* (2007) numerically computed a translatory wave down the Markarfljót valley using equations derived from the two dimensional St. Venant's equations. Their conclusions were among other, that the Manning's *n* could change considerably with depth although Chézy's *C* (see § 3.3) would remain constant.

Roberts and Gudmundsson (2015) show that the initial composition of floodwater during the 1362 and 1727 jökulhlaups was hyperconcentrated, having a sediment-by-volume fraction as high as 60% at the beginning of the floods. From contemporary observations of volcanogenic jökulhlaups (Magnússon *et al.*, 2012a), such flow conditions would apply to the initial propagation of the flood. More fluidal flows would be expected following the initial wave front.

Given the large uncertainty about flow rheology, Manning's *n* values in this study have been split into three intervals, similar to the approach by Hákonardóttir *et al.* (2005):

- Low Manning's hypothesis: $n = 0.05$
- Medium Manning's hypothesis: $n = 0.10$
- High Manning's hypothesis: $n = 0.15$

3.2.2. Topographic envelope

A 5 m cell-size Digital Surface Model (DSM) covering the Öræfajökull ice-cap and a significant portion of the surrounding non-glaciated areas was used as the topographic envelope for the hydraulic simulations

(Figure IV-4). The DSM is derived from an airborne LiDAR survey performed by TopScan GmbH during the summers of 2011 and 2012. The vertical accuracy of the LiDAR measurements and the average density of the point cloud are estimated <0.5m and ~0.33point/m^2, respectively (Jóhannesson *et al.*, 2011; Jóhannesson *et al.*, 2013). Hydro-enforcement of the glacial part of the DSM was performed to ensure that water would not be trapped in crevasses. In turn, bridges and buildings in the non-glaciated area were not removed. In order to reduce the use of computational resources and optimize stability during simulations, spatial subsets of the LiDAR-derived DSM were used. Each subset extends from one release area or more, upstream, to portions of ocean or of active *sandar* downstream (Figure IV-4).

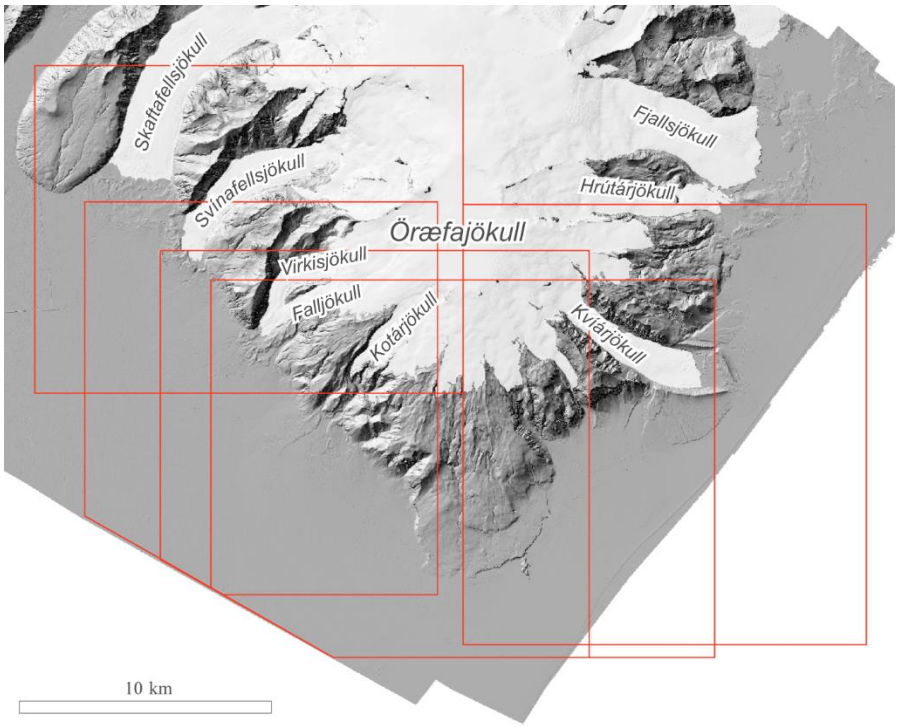

Figure IV-4: Extent of the LiDAR DSM (Öræfajökull and surrounding non-glaciated areas) used in the hydraulic simulations. The rectangles show spatial subsets of the DSM.

3.2.3. Release areas, maximum discharge, and initial flow depth

Ten areas were delineated, from which floods due to caldera eruptions, flank eruptions, and pyroclastic flows were released (Figure IV-5). The lower boundary of the release areas corresponding to a caldera eruption was placed at ~1,500 m AMSL. At this elevation, subglacial floodwater flowing down from the caldera is expected to burst onto the glacier surface, as ice thicknesses are only ~50 – 100 m, as estimated by Magnússon *et al.* (2012b). The lower boundary of the release areas for floods caused by the formation of pyroclastic density currents was placed at a distance of 1–2.8 km from the caldera rim. The release areas corresponding to floods caused by flank eruptions were delineated to enclose the hypothetical eruptive fissures (Figure IV-2) proposed by Gudmundsson *et al.* (2015).

The mean slope angle in the release areas varies between 14° and 24.5° (Figure IV-6). For each scenario, iterative runs were performed to determine the initial flow depth (Figure IV-6) in the release areas necessary to reach the predefined maximum discharge (Table IV-1) at the cross-sections near to the glacier margins.

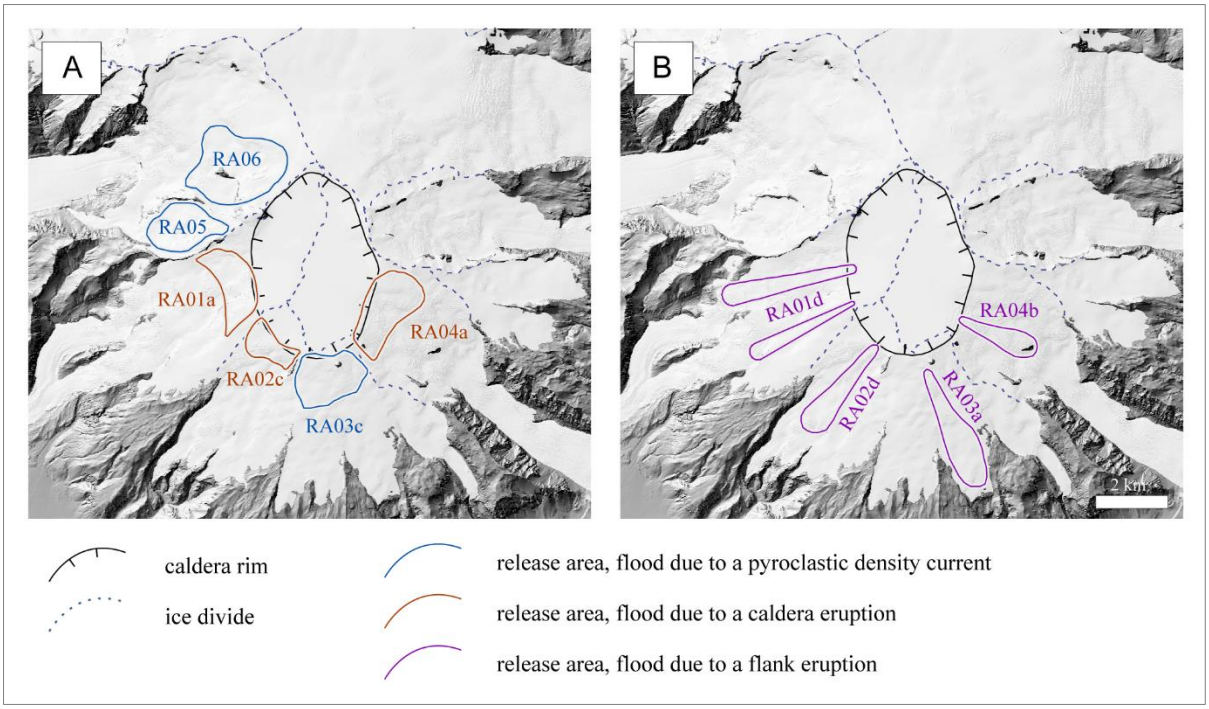

Figure IV-5: Flood release areas in the case of pyroclastic density currents (A), caldera eruption (A), and flank eruptions (B). Delineation of the caldera rim is derived from ice thickness estimations by Magnússon et al. (2012b). Flood release areas in the case of flank eruptions (B) enclose the hypothetical eruptive fissures (Figure IV-2) proposed by Gudmundsson et al. (2015).

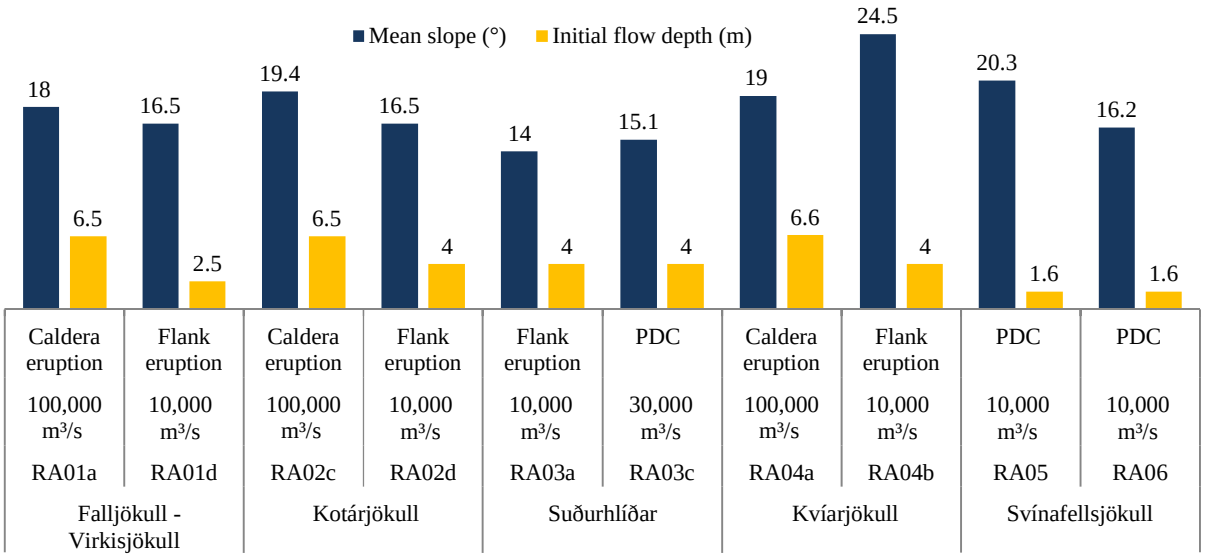

Figure IV-6: Mean slope (°) of the release areas and corresponding initial flow depth (m) necessary to match the required maximum discharge at the downstream cross-sections.

3.3. Equations of motion

The SAMOS model solves numerically the two dimensional depth averaged St. Venant's equations. One can choose between several different bed friction models but the Manning equation is not an option. Of the models available in SAMOS the Chézy's friction model is the most appropriate to simulate fluid flow in jökulhlaups. In the Chézy's model the shear stress, τ_b, is dependent on the mean speed of the fluid, u, according to

$$\tau_b = \rho C_{dyn} u^2,$$

where ρ is the density of the fluid, and C_{dyn} is a dynamic friction coefficient that needs to be determined. It should be noted that the SAMOS model finds the time dependent speed unlike the traditional Chézy's equation for a steady, open channel turbulent flow where the speed is described by

$$u = C\sqrt{RSg},$$

where R is the hydraulic radius of the channel, S is the slope of the energy grade line, C is a dimensionless friction parameter often called Chézy's C and g is gravitational acceleration.

3.3.1. Dynamic friction

We assume that friction is the same for the transient case as for the steady state case so exploring the friction of the steady state case is sufficient. Consider a cross section of a hill that is tilted θ degrees from horizontal (Figure IV-7). When steady state is reached the force balance on a small unit is:

$$\rho g \sin(\theta) = \frac{\tau_b}{h},$$

where ρ is the density of the fluid, g is gravity, τ_b is the shear stress and h is the height of the unit (flow depth in our case). The shear stress using the Chézy's friction model was given above as

$$\tau_b = \rho C_{dyn} u^2,$$

where u is the mean speed of the fluid and C_{dyn} is the dynamic friction coefficient that needs to be determined. If the Chézy's friction model is written in terms of this dynamic frictional coefficient the speed becomes

$$u = \sqrt{\frac{hg\sin(\theta)}{C_{dyn}}},$$

or the frictional coefficient is

$$C_{dyn} = \frac{g \sin(\theta) h}{u^2}.$$

If we chose to use the Chézy's equation for the steady state speed (as given above) and note that the flow is thin (i.e. $h \ll b$ where h is the flow depth and b is the width of the flow) so the hydraulic radius is

$$R = \frac{hb}{b+2h} \to h,$$

and the flow is uniform so $S = sin(\theta)$, where θ is the slope of the channel (see Figure IV-7), the relationship between the dynamic friction coefficient, C_{dyn}, and Chézy's, C, is

$$C_{dyn} = \frac{1}{C^2}.$$

Therefore, with a given Chézy's, C, the dynamic friction coefficient, C_{dyn}, (as needed by SAMOS) could be found.

The use of Manning's equation is more common when describing uniform, steady open channel flow. In Manning's equation the mean speed is given by

$$u = \frac{1}{n} R^{2/3} S^{1/2},$$

where n is an empirical Manning coefficient, R is the hydraulic radius of the channel (again for thin flow $R \approx h$) and S is again the slope of the energy grade line (for uniform flow $S = sin(\theta)$). The dynamic friction coefficient, C_{dyn}, may then be written in terms of Manning's resistance coefficient, n, by

$$C_{dyn} = \frac{n^2 g}{h^{1/3}}.$$

Therefore, with a given Manning's n coefficient and given initial flow depth the dynamic friction coefficient, C_{dyn}, (as needed by SAMOS) can be found.

In SAMOS the dynamic friction coefficient, C_{dyn}, is set to the same value in the whole domain. This is, therefore, equivalent to setting the Chézy's *C* to the same value in the whole domain but the Manning's *n* will vary with depth (the values given are averaged Manning values). Choosing a constant Chézy's *C* within the whole domain has been shown to be more realistic in jökulhlaups than choosing a constant Manning's *n* in the whole domain (Elíasson *et al.*, 2007). Since the literature on Manning's *n* in jökulhlaups is greater than on Chézy's *C*, Manning's *n* values will be referred to in all scenarios listed below instead of the Chézy's *C*. The interested reader can refer to the equations above if the values of Chézy's *C* are preferred.

3.3.2. Initial flow depth

An estimate of the discharge of the flow is given by $Q = uhb = \frac{1}{n}R^{5/3}S^{1/2}b$ so the flow depth is

$$h = \left(\frac{nQ}{S^{1/2}b}\right)^{3/5}.$$

When determining the initial flow depth in the release area, the desired Manning's *n* coefficients and the desired maximum discharge at predefined cross-sections need to be specified. The mean angle of the slope can be found from the DSM and an estimate of the length of the cross-section can also be made. The actual initial flow depth in the release area can only be found with an iterative process where one initial flow depth is tested and the maximum discharge at the glacier edge is calculated. If the maximum discharge is not as desired, the initial flow depth is increased if the discharge is too low and decreased if the discharge is too high. This process is repeated until the maximum discharge reaches the desired value.

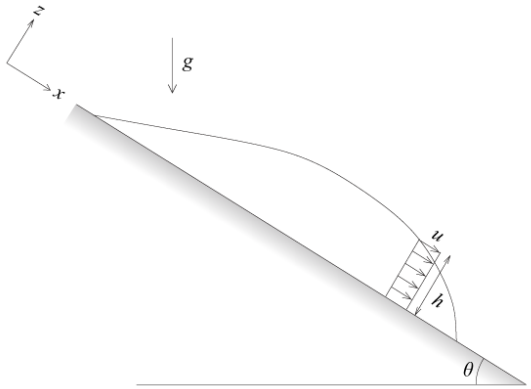

Figure IV-7: The slope and the coordinates in SAMOS.

3.4. Computations and visualisation

Inundation extent, flood depths, and flow speeds were computed for every scenario along with minimum surface transport times and exported to 10 m cell-size grids.

3.4.1. GIS post-processing

The output grids were finally post-processed in a Geographic Information System (GIS). Four thematic mosaics were produced, i.e. one mosaic per model output (inundation extent, depths, flow speeds, and travel times), such as to provide an overall picture of the flood area. For each model output, modelling results for Manning's *n* 0.05 and 0.10 were combined. For the depths of flooding and flow speeds, the output rasters were merged to extract the maximum values found for every cell within the modelling domain. For the surface transport times, in turn, the output grids were merged such as to determine the minimum values at peak discharge.

3.4.2. Planned use

Maximum flood depths and maximum flow speeds were extracted to serve as input for rating flood hazards (Pagneux and Roberts, 2015), and in an assessment of the populations exposed to floods (Pagneux, 2015a) along with results on inundation extent.

Minimum surface transport times were processed to be used along with estimates of

eruption onset time, subglacial retention time, and subglacial transport time (Gudmundsson *et al.*, 2015) in an assessment of the time available for evacuating the areas at risk of flooding (Pagneux, 2015b).

4. Results

4.1. Inundation extent

4.1.1. Individual simulations

Figures IV-8 to IV-17 show the results of the individual simulations. The principal findings regarding the inundation extent, as estimated from the simulations, are:

- The use of an average Manning's *n* 0.15 led to an underestimation of the inundation extent in the areas flooded in 1362 and 1727 as estimated by Roberts and Gudmundsson (2015). Simulation results using Manning's *n* 0.15 were, therefore, not used.
- On the alluvial fans, little difference in extent was found between Manning's *n* 0.05 and Manning's *n* 0.10 scenarios (e.g. Figure IV-10). Since the simulations were stopped after a time interval ranging 15,000 – 50,000 seconds, it can be considered that Manning's *n* 0.05 scenarios portray, "in advance", the inundation extent that the 0.10 scenarios reach at a later point in time.
- The simulated floods were individually large enough to inundate the entire alluvial fan at the base of the glaciers from which floodwater originate. Flood extent was eventually constrained by adjacent, overlapping fans. Where floodwater interacted with an adjacent fan, the extent of floodwater run-up was often considerable, ranging 500 – 800 m at some locations with Manning's *n* set to 0.05 (Figure IV-18).

4.1.2. Overall area at risk of flooding

Superimposition of the individual simulations results indicate that 237 km^2 are at risk of flooding (Figure IV-19). From an analysis of LiDAR-derived hillshades and aerial imagery, one can add to the flood area identified in the simulations about 110 km^2 of *sandar*, to the south (Skeiðarársandur) and to the east (Breiðamerkursandur). The Skaftafellsá river marks, to a significant degree, the limit of the flood area to the west as little water is shown to flow over the highway to Skaftafell, near the junction with the National road. The estuary of the Breiðá and Fjallsá rivers is the likely limit of the flood area to the east.

4.1.3. Inundation extent after risk source

Of the 347 km^2 of land identified at risk of flooding (simulations and photointerpretation), 284 km^2 (82%) were found exposed to floods caused by a caldera eruption, flank eruptions, or pyroclastic density currents, 42 km^2 (12%) to floods caused by flank eruptions or pyroclastic density currents, and 21 km^2 (6%) to floods caused by pyroclastic density currents only (Figure IV-19).

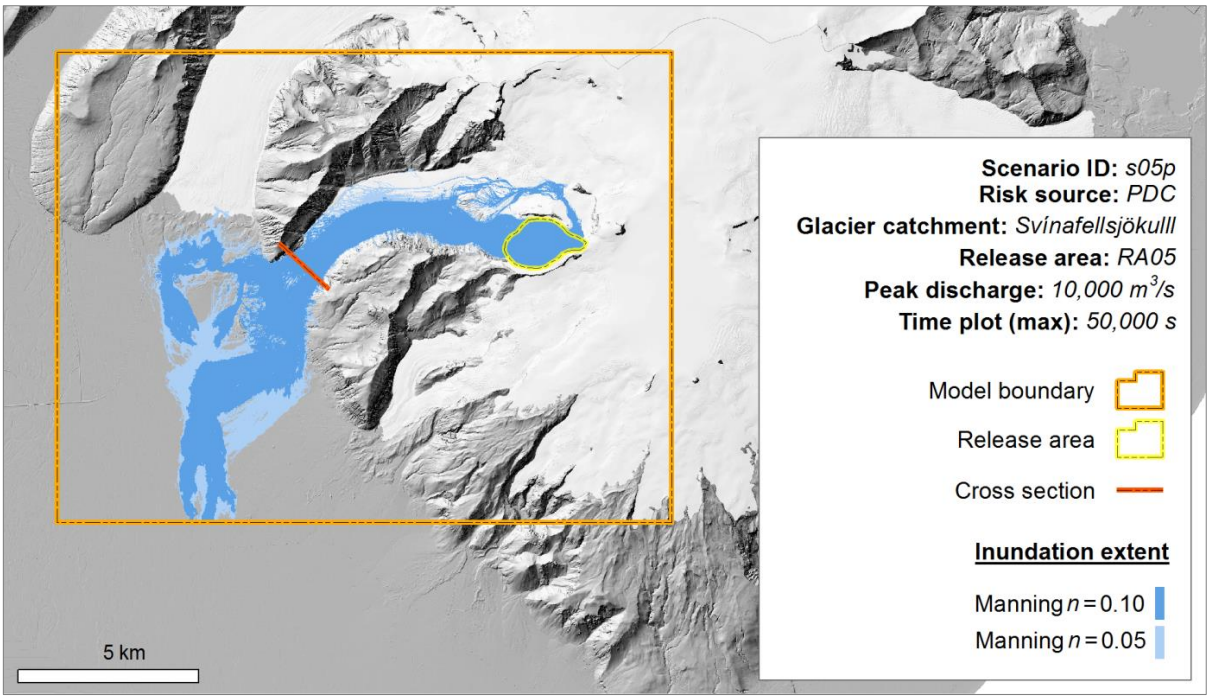

Figure IV-8: Inundation extent of a 10,000 m^3/s peak discharge flood caused by a pyroclastic density current in the Svínafellsjökull glacier catchment, south from the Svínafellshryggur ridge. Extent of inundation is shown for Manning's n 0.05 and 0.10 after 50,000 s.

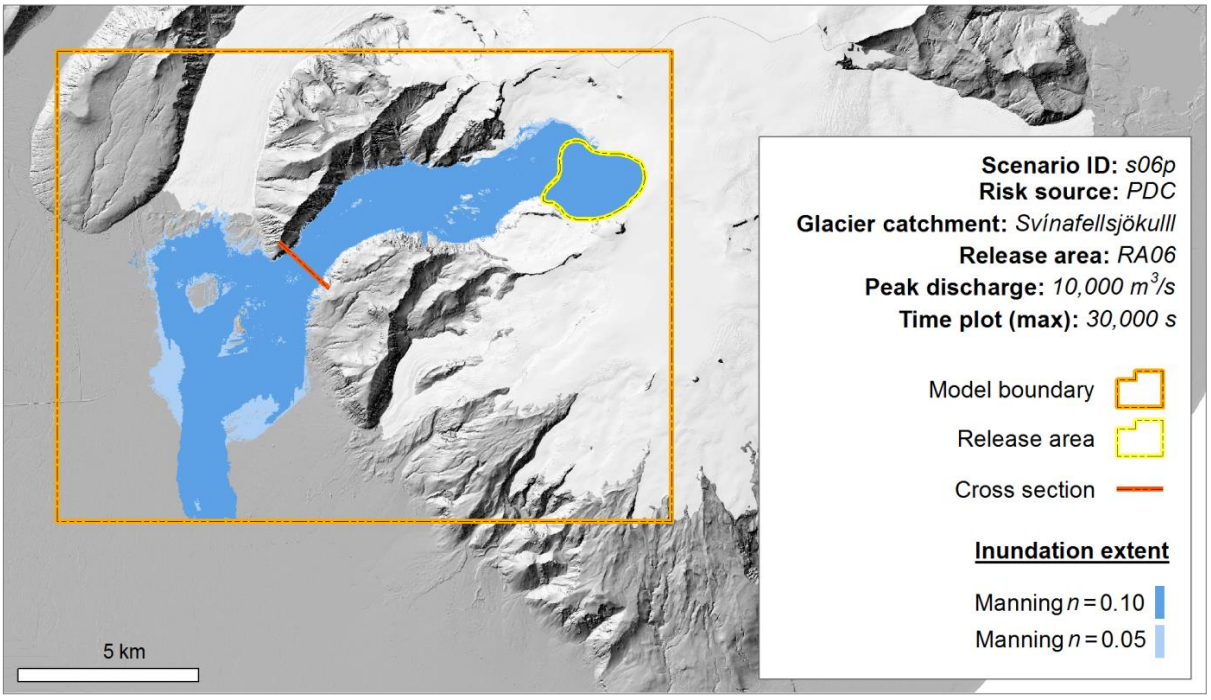

Figure IV-9: Inundation extent of a 10,000 m^3/s peak discharge flood caused by a pyroclastic density current in the Svínafellsjökull glacier catchment, north from the Svínafellshryggur ridge. Extent of inundation is shown for Manning's n 0.05 and 0.10 after 30,000 s.

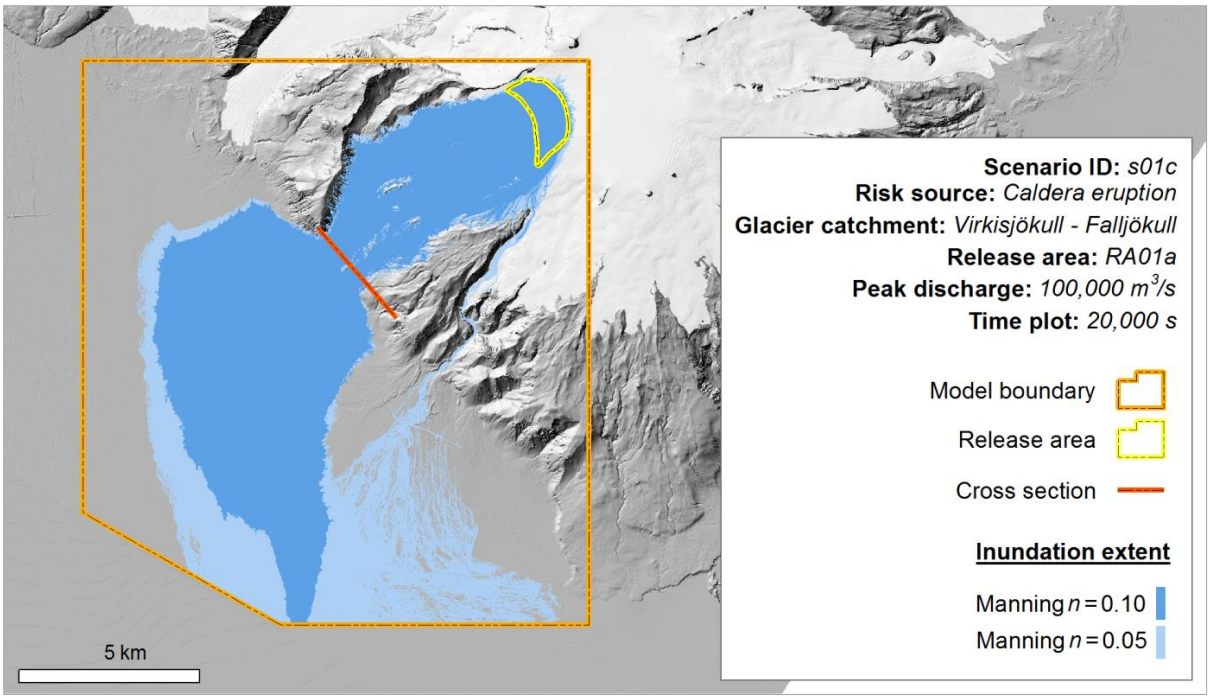

Figure IV-10: Inundation extent of a 100,000 m^3/s peak discharge flood in the Virkisjökull – Falljökull glacier catchment, caused by a caldera eruption. Extent of inundation is shown for Manning's n 0.05 and 0.10 after 20,000 s.

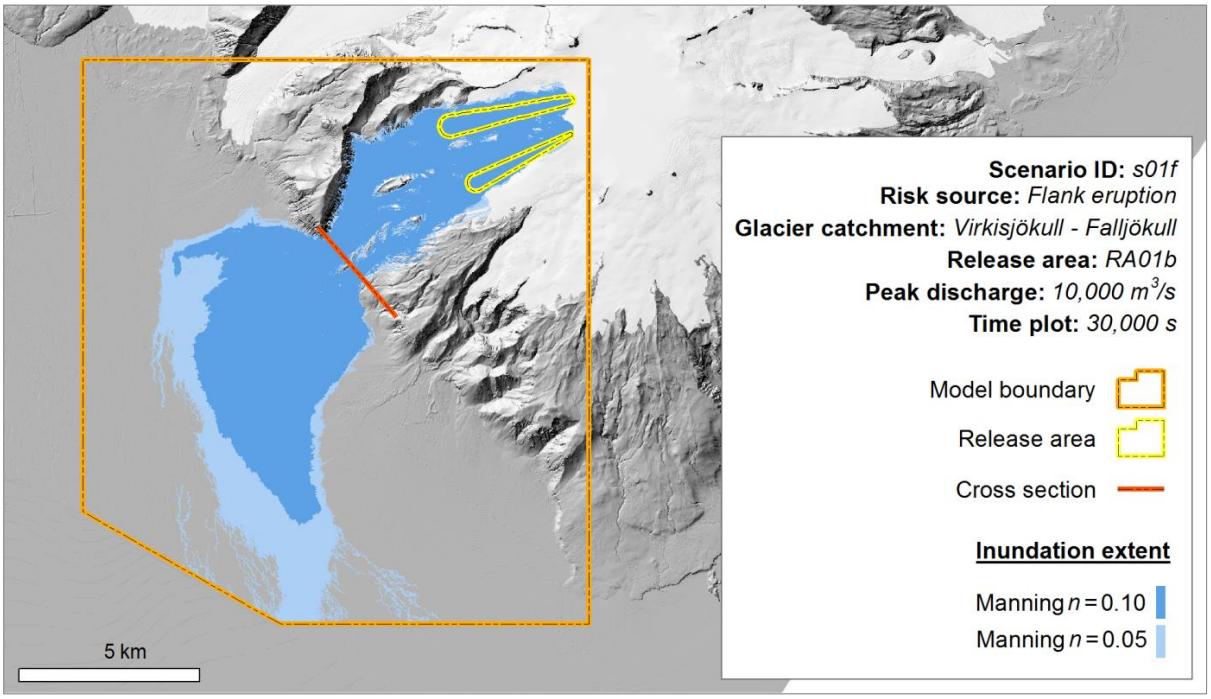

Figure IV-11: Inundation extent of a 10,000 m^3/s peak discharge flood in the Virkisjökull – Falljökull glacier catchment, caused by a flank eruption. Extent of inundation is shown for Manning's n 0.05 and 0.10 after 30,000 s.

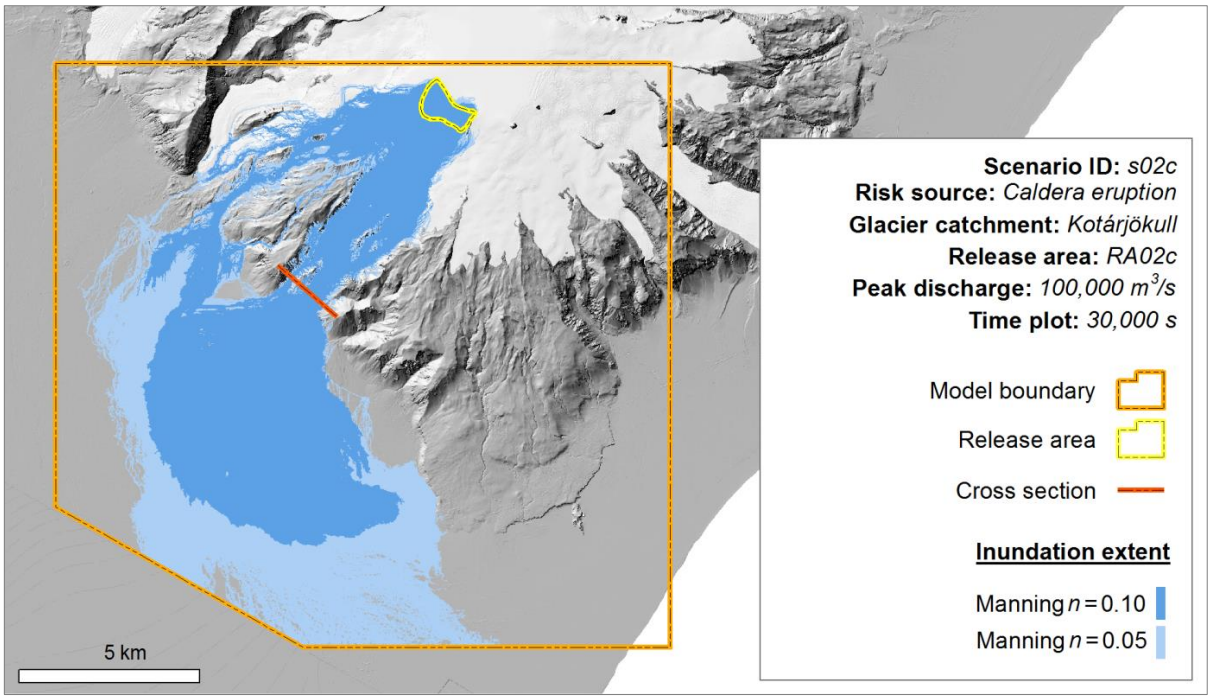

Figure IV-12: Inundation extent of a 100,000 m^3/s peak discharge flood caused by an eruption in the caldera that affects the Kotárjökull glacier catchment. Extent of inundation is shown for Manning's n 0.05 and 0.10 after 30,000 s.

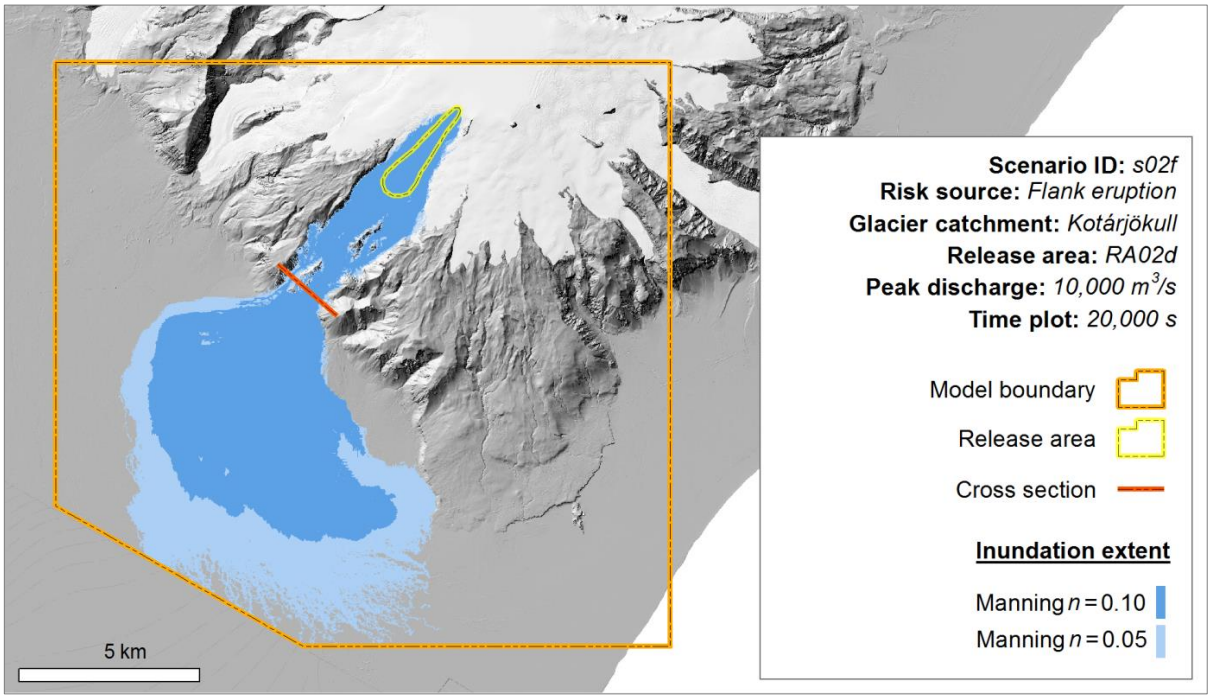

Figure IV-13: Inundation extent of a 10,000 m^3/s peak discharge flood caused by a flank eruption that affects the Kotárjökull glacier catchment. Extent of inundation is shown for Manning's n 0.05 and 0.10 after 30,000 s.

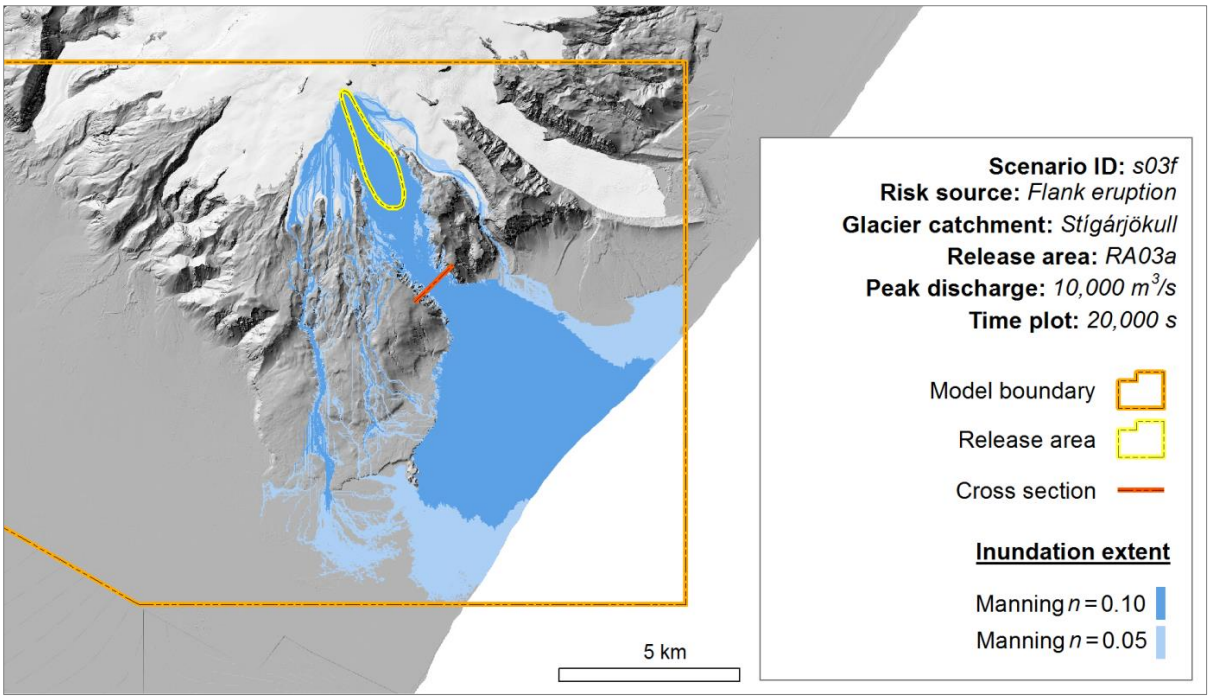

Figure IV-14: Inundation extent of a 10,000 m^3/s peak discharge flood caused by a flank eruption that affects the Stigárjökull glacier catchment. Extent of inundation is shown for Manning's n 0.05 and 0.10 after 20,000 s.

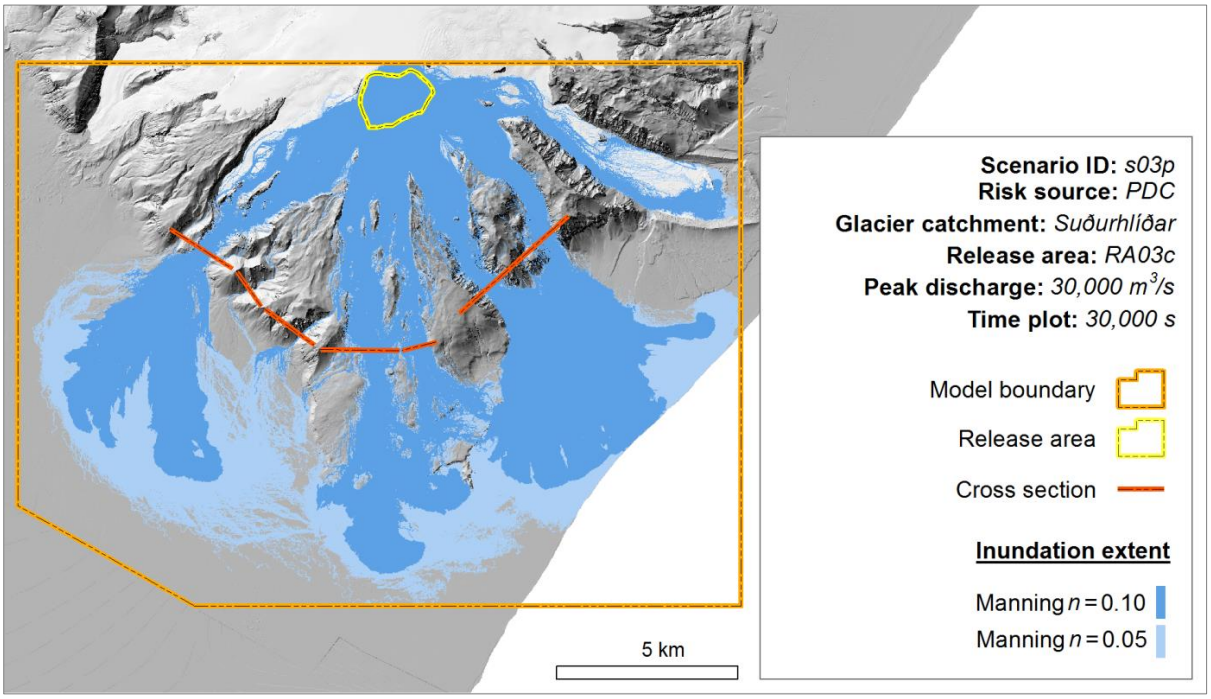

Figure IV-15: Inundation extent of a 30,000 m^3/s peak discharge flood caused by the formation of a pyroclastic density current in the Stigárjökull drainage area. Extent of inundation is shown for Manning's n 0.05 and 0.10 after 30,000 s.

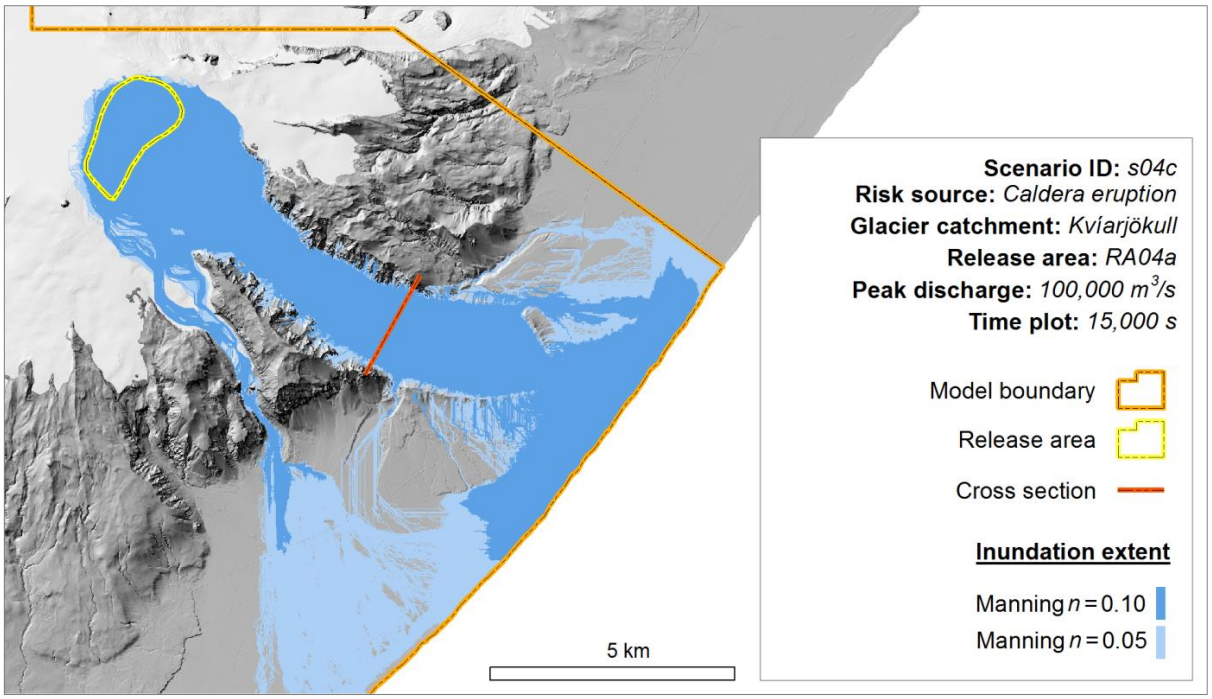

Figure IV-16: Inundation extent of a 100,000 m^3/s peak discharge flood caused by an eruption in the caldera that affects the Kvíárjökull glacier catchment. Extent of inundation is shown for Manning's n 0.05 and 0.10 after 15,000 s.

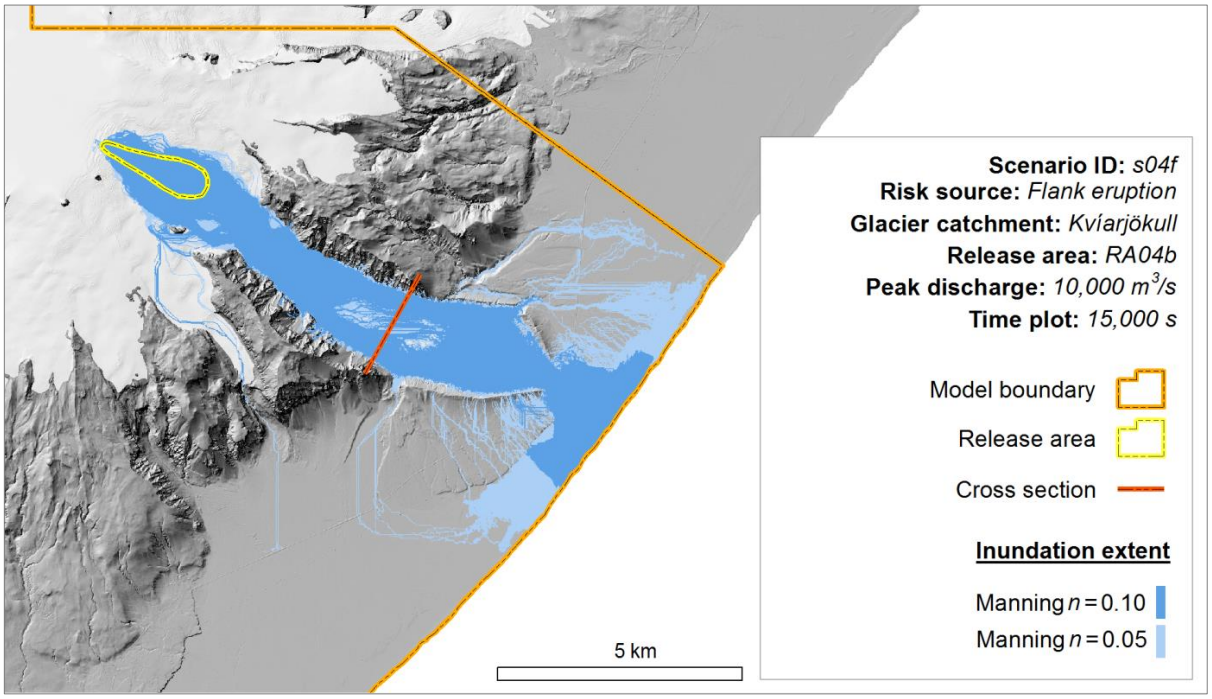

Figure IV-17: Inundation extent of a 10,000 m^3/s peak discharge flood caused by an eruption in the caldera that affects the Kvíárjökull glacier catchment. Extent of inundation is shown for Manning's n 0.05 and 0.10 after 15,000 s.

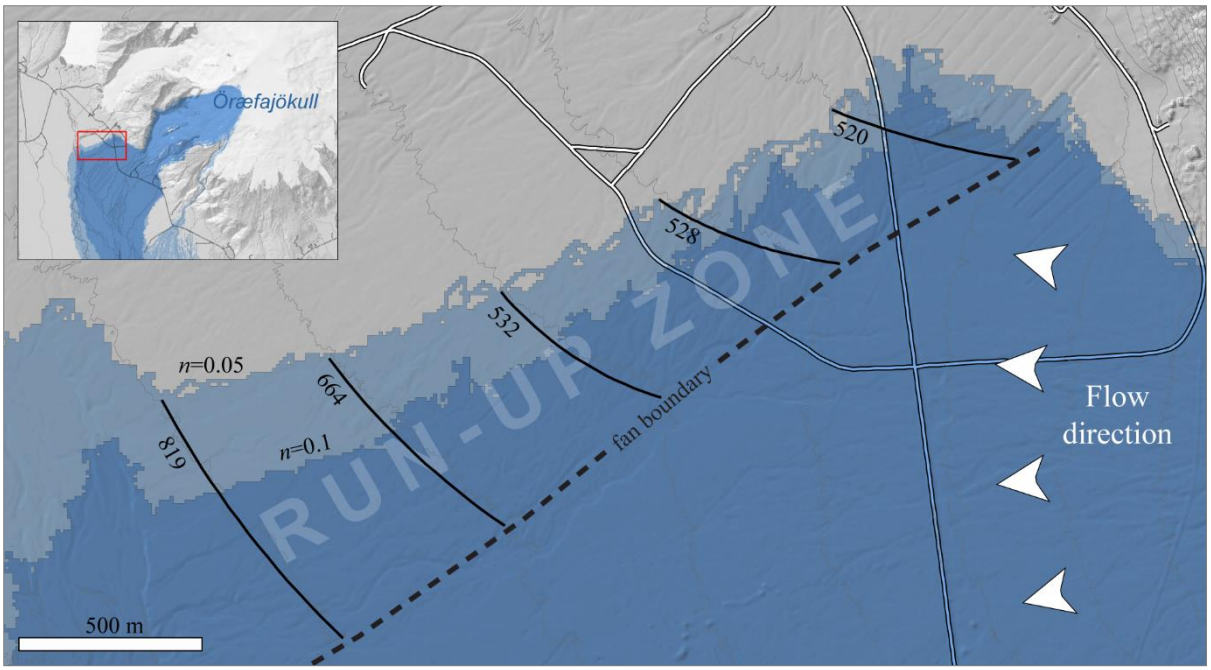

Figure IV-18: Run-up distances (m), onto adjacent alluvial fan to the north, of floodwater propagating on the Virkisá alluvial fan. The scenario is a 100,000 m^3/s flood initiated in the Virkisjökull-Falljökull glacier catchment, with Manning's n set to 0.05 and 0.10. Run-up distances (solid lines) are estimated from the boundary between fans (dashed line), based on constant elevations (contour lines in grey).

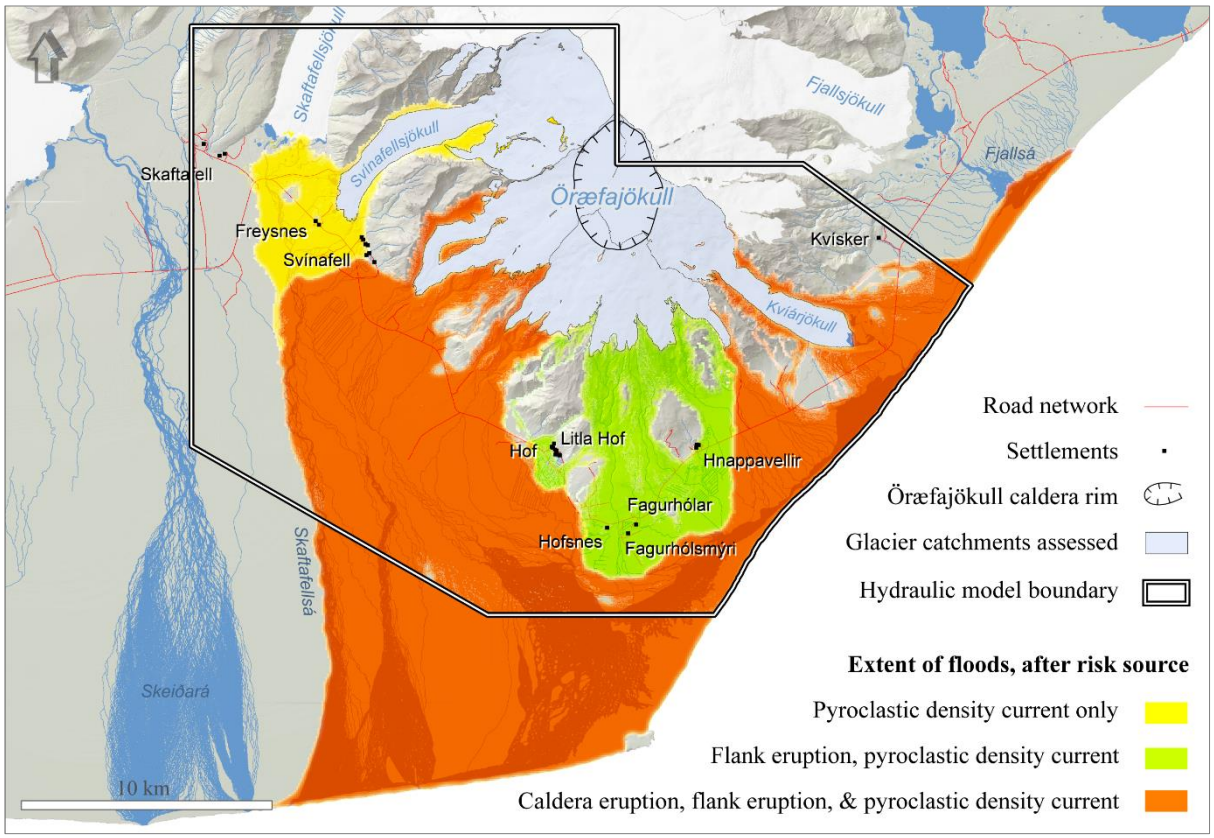

Figure IV-19: Areas at risk of flooding after superimposition of the individual simulations results and photointerpretation of the landscape beyond the spatial boundary of the numerical model.

4.2. Depths of flooding

On average, the maximum depths of flooding found in the proglacial area were ~4.5 m. Maximum flood depths in excess of 10 m were found in nearly 20% of the flooded area, mostly along the main axes of flow propagation (Table IV-4, Figure IV-20). Sectors where the maximum depths were below 0.50 m are much more limited in extent, representing only 12% of the area identified at risk of flooding.

Table IV-4: Extent of maximum flood depths in proglacial areas (Manning's n 0.05 and 0.10 combined).

Maximum depths (m)	Extent (km^2)	Extent (%)
< 0.5	28	12
0.5–1	23	10
1–2	29	12
2–5	84	35
5–10	45	19
> 10	28	12

4.3. Flow speeds

Maximum flow speeds in excess of 3 m/s were found on ~200 km^2 of non-glaciated terrains (Table IV-5, Figure IV-21).

On average, the maximum flow speeds found within the whole modelled domain ranged from 12 to 28 m/s (43 to 100 km/h). This range of values, which applies to the slopes of the volcano and to the lowland as one, should not be regarded as extravagant. If one considers the peak discharge of floods and the distance from the source of timing at which the average front speeds were estimated, the results on speeds are indeed in good accordance with empirical observations made for lahars triggered by the 1926 eruption of Mount Tokachi and the Mount St. Helens 1980 eruption (Pierson, 1998; Table IV-6). On the slopes of the volcano (above 100 m AMSL), which are characterised by a mean slope angle of 22.7° (~42%), the average flow speeds ranged 22 – 42 m/s.

Table IV-5: Extent of maximum flow speeds in proglacial areas (Manning's n 0.05 and 0.10 combined).

Maximum flow speeds (m/s)	Extent (km^2)	Extent (%)
< 3	35	15
3–5	12	5
5–10	72	31
10–20	54	23
> 20	64	27

4.4. Surface transport times

4.4.1. Transport time at maximum discharge

Minimum surface transport times from the lower boundaries of the release areas down to the National Road ranged between 4 minutes, downstream of Stigárjökull, and 51 minutes at the foot of Svínafellsjökull (Figure IV-22). Manning's *n* 0.05 scenarios yielded transport times half the transport times of Manning's *n* 0.10 scenarios; the lower the Manning's *n*, the shorter the transport times.

As the lower boundary of the release areas for floods due to a flank eruption are close to the glacier margins, the surface transport times of the corresponding floods were found to be identical or very similar in some glacier catchments (e.g. Kotárjökull, Virkisjökull-Falljökull) to the transport times of floods due to a caldera eruption. For floods due to a flank eruption, the proximity of the release areas to the lowland compensated, to a significant degree, for less discharge.

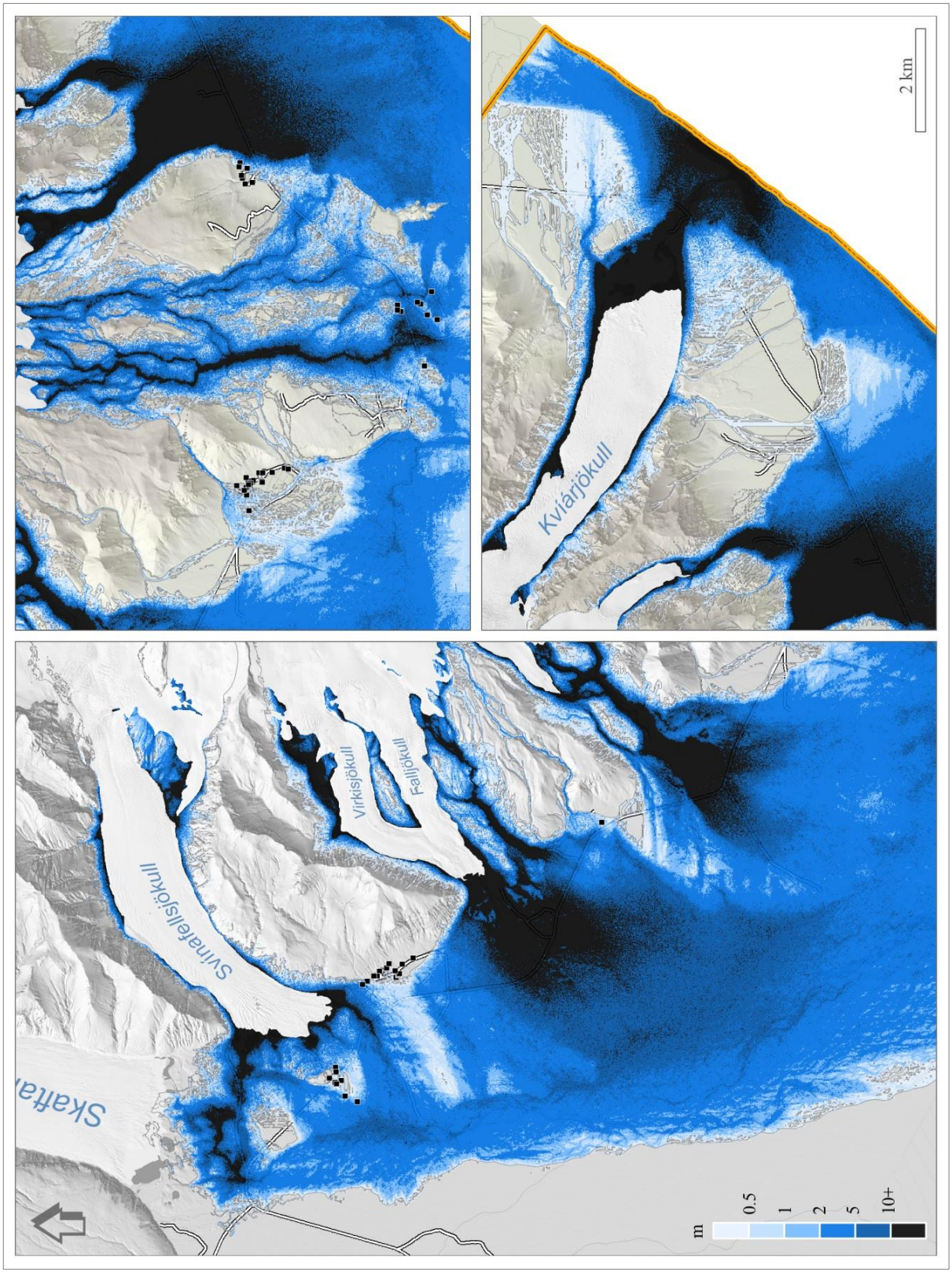

Figure IV-20: Aggregated maximum depths of flooding (Manning's n 0.05 and 0.10 combined). Depths in excess of 10 m cover nearly 20% of the flooded area, mostly along the main axes of flow propagation. Settlements are shown as black dots.

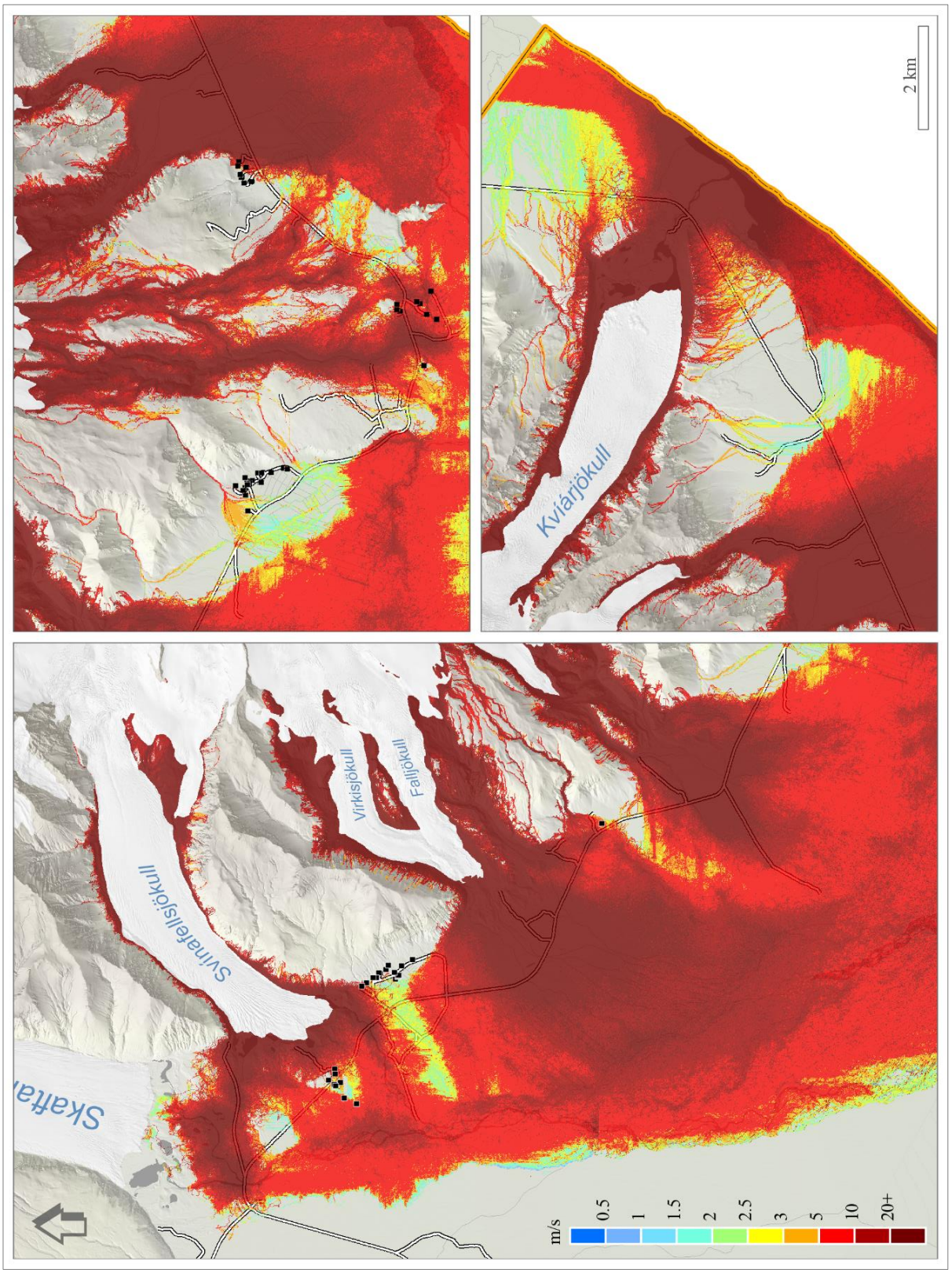

Figure IV-21: Aggregated maximum flow speeds (Manning's n 0.05 and 0.10 combined). Speeds in excess of 3m/s are found on 85% of the flood area. Settlements are shown as black dots.

Table IV-6: Average front speeds of floods caused by pyroclastic density currents during volcanic eruptions of Mount Tokachi (1926) and Mount St. Helens (1980). After Pierson (1998).

Event: location (year)	Distance from source of timing (km)	Average front speed from source of timing (m/s)	Peak discharge nearest source (m^3/s)	Risk source	Type of flood
Mount St. Helens: Pine Creek (1980)	4.4	35.7	50,000–100,000	Pyroclastic surge/flow	Debris flow
Mount St. Helens: South Fork Toutle River (1980)	4	38	68,000	Pyroclastic surge/flow	Debris flow, hyperconcentrated flow
Mount Tokachi: Huranogawa (1926)	2.4	42.1	14,800 at 8 km	Pyroclastic surge/flow	Debris flow

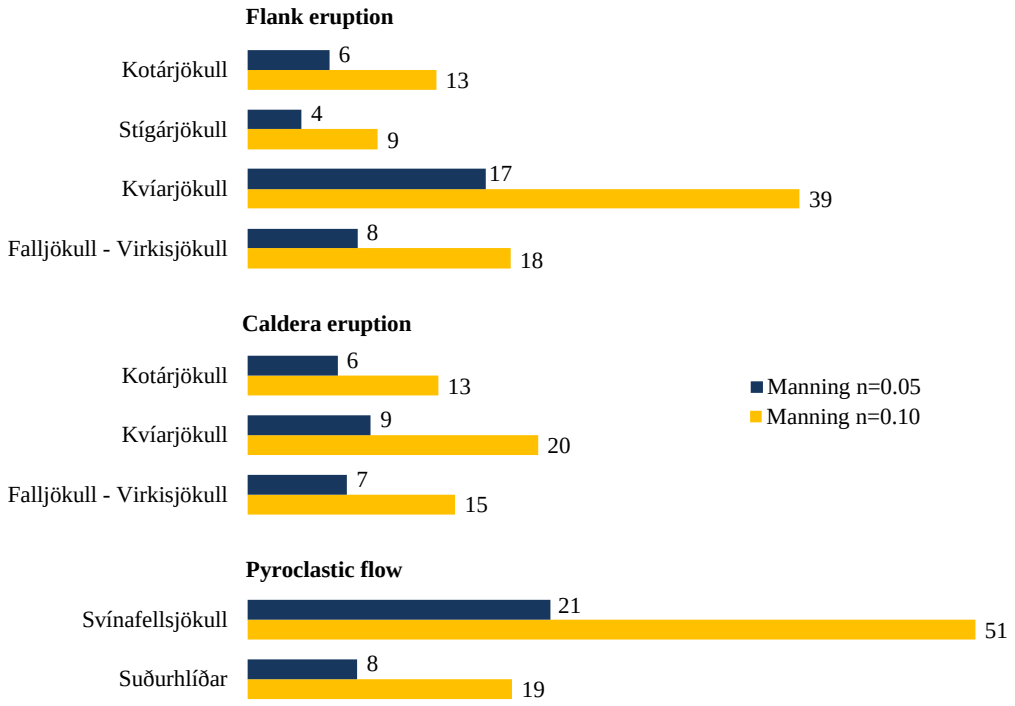

Figure IV-22: Floodwater surface transport times (min.) at peak discharge, from the lower boundaries of the release areas down to the national road.

4.4.2. Time available from the onset of supraglacial flow

The transport times at maximum discharge cannot be considered the equivalent of the time effectively available from the true onset of the floods without further investigation of the concentration phase. Gudmundsson *et al.* (2015) suggest for catastrophic floods caused by a caldera eruption of Öræfajökull Volcano an approximate rising rate in the form of $Q = At$, where Q is discharge, A = 55 m^3/s^2 and t the time from flood onset (Figure IV-23). At such a rate, it takes 30 minutes to reach a 100,000 m^3/s discharge but 3 minutes only to reach 10,000 m^3/s.

Simulation of a flood affecting the Virkisjökull-Falljökull glacier catchment indicates a 31-minute time down to the national road at input discharge 10,000 m^3/s and Manning's *n* set to 0.10, which is twice as long as at discharge 100,000 m^3/s (increase factor ~2). Using A = 55 m^3/s^2 as an assumption, floodwater at discharge 10,000 m^3/s is expected to reach the National road after 34 minutes following the flood onset while it does take 45 minutes for floodwater at 100,000 m^3/s (Table IV-7).

How surface transport times computed in SAMOS can be used in an estimation of the time effectively available from the onset of floods at the glacier surface is further addressed in chapter VII (Pagneux, 2015b).

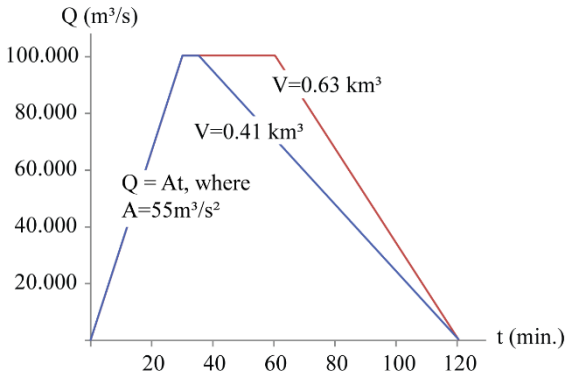

Figure IV-23: Hydrograph of possible catastrophic jökulhlaups (meltwater volumes of 0.41 km^3 and 0.63 km^3) caused by a caldera eruption of Öræfajökull Volcano (after Gudmundsson et al., 2015). Rising rate in the concentration phase is approximated as $Q = At$ (where Q is discharge, A = 55m^3/s^2 and t the time from flood onset).

Table IV-7: Minimum transport time at maximum discharge and time available from flood onset, using as assumptions a rising rate Q = At where A = 55m^3/s^2 and an increase factor of ~2 in transport time between a 10,000 m^3/s discharge and a 100,000 m^3/s discharge.

Rising limb	Discharge (m^3/s)	Time elapsed from onset of supraglacial flow (min.)	Minimum transport time computed in SAMOS (min.)	Time available, from onset of supraglacial flow(min.)
Intermediate	10,000	3	31	34
Peak	100,000	30	15	45

5. Summary

Jökulhlaups resulting from subglacial volcanism at Öræfajökull have been modelled as viscous fluids using the SAMOS numerical model. Input data for the modelling were derived from ten estimates of maximum discharge for three eruptive processes (i.e. risk sources): caldera eruption, flank eruptions, and pyroclastic density currents. Because of the wide range of likely flow rheologies, three Manning's *n* values were assessed: 0.05, 0.1, and 0.15.

In each SAMOS simulation, predetermined volumes of water were released instantaneously from elevations where floodwater is expected to break through the surface of the ice-cap during a volcanogenic jökulhlaup (Gudmundsson *et al.*, 2015; Roberts and Gudmundsson, 2015). The resulting supraglacial cascade of floodwater was then modelled and a series of temporal snapshots of model output created, allowing inferences about inundation extent, maximum depths of flooding, maximum flow speeds, and minimum surface transport times. The main findings of the study can be summed up in the following points:

- A total of 237 km^2 of non-glaciated terrains, limited to the west by the Skaftafellsá river and to the east by the Breiðá river, was identified at risk of flooding within the spatial boundaries of the hydraulic model (Figure IV-8 to Figure IV-19). From an analysis of LiDAR-derived hillshades and aerial imagery, one can add to the flood area identified in the simulations about 110 km^2 of sandur, to the south (Skeiðarársandur) and to the east (Breiðamerkursandur).

- Shallow waters (< 0.5 m) were found in only one-tenth of the flooded area (Figure IV-20). Maximum flood depths in excess of 10 m were found along the main axes of flow propagation (20% of the flood area).

- The proglacial area is mainly affected by maximum flow speeds in excess of 3 m/s (Figure IV-21). On average, the maximum flow speeds found within the whole modelled domain ranged from 12 to 28 m/s (22 to 42 m/s on the slopes of the volcano).

- At maximum discharge, the minimum surface transport times to the National Road ranged between 4 minutes, downstream Stigárjökull, and 51 minutes, at the foot of Svínafellsjökull (Figure IV-22). These transport times are not an equivalent of the time effectively available from the onset of floods at the glacier surface. They can be used, however, in an estimation of the time available for evacuation, as addressed in chapter VII (Pagneux, 2015b).

Entrainment of ice during a high-magnitude jökulhlaup remains arguably one of the greatest unknown factors. Historical accounts of the 1727 jökulhlaup (Thorarinsson, 1958) imply that vast quantities of glacier ice were transported as floodwater descended onto the *sandar* (Roberts and Gudmundsson, 2015); this also implies that ice release was prevalent during the 1362 jökulhlaup. A high concentration of fragmented ice would cause floodwater bulking, which would affect the rheology of the flow and even the routing of floodwater, especially where temporary ice-jams formed. Such factors could not be addressed computationally in this study, but they should be kept in mind when a use is made of the simulations results in a damage potential assessment (Chapter V) and the estimation of the time available for evacuation (Chapter VII).

6. Acknowledgements

The authors would like to thank Magnús Tumi Gudmundsson, Kristín Martha Hákonardóttir, Tómas Jóhannesson, and Trausti Jónsson for their review and proof-reading of the chapter.

The present work was funded by the Icelandic Avalanche Mitigation Fund, the National Power Company, and the Icelandic Road and Coastal Administration.

7. References

Atapattu, D. D., Chhabra, R. P., & Uhlherr, P. H. (1995). Creeping sphere motion in Herschel-Bulkley fluids: Flow field and drag. *J. Non-Newt. Fluid Mech., 59*, 245–265.

Bagnold, R. A. (1954). Experiments on a gravity free dispersion of large solid spheres in a Newtonian fluid under shear. *Proc. R. Soc. London, A 225*, 49–63.

Bingham, E. C. (1916). An Investigation of the Laws of Plastic Flow. *U.S. Bureau of Standards Bulletin, 13*, 309–353.

Bingham, E. C., & Green, H. (1919). Paint, a plastic material and not a viscous fluid; the measurement of its mobility and yield value. *Proc. Am. Soc. Test. Mater., 19*, 640–664.

Björnsson, H. (1992). Jökulhlaups in Iceland: prediction, characteristics, and simulation. *Annals of Glaciology, 16*, 96–106.

Brunner, G. W. (2010). *HEC-RAS River Analysis System, User's Manual Version 4.1.* US Army Corps of Engineers, Hydrologic Engineering Center.

Capra, L., Norini, G., Groppelli, G., Macias, J. L., & Arce, J. L. (2008). Volcanic hazard zonation of the Nevado de Toluca volcano, Mexico. *Journal of Volcanology and Geothermal Research, 176*(4), 469–484.

Charbonnier, S. J., Germa, A., Connor, C., Gertisser, R., Preece, K., Komorowski, J. C., Lavigne, F., Dixon, T., and Connor, L. (2013). Evaluation of the impact of the 2010 pyroclastic density currents at Merapi volcano from high-resolution satellite imagery, field investigations and numerical simulations. *Journal of Volcanology and Geothermal Research, 261*, 295–315.

Charbonnier, S., & Gertisser, R. (2009). Numerical simulations of block-and-ashflows using the Titan2D flow model: examples from the 2006 eruption of Merapi Volcano, Java, Indonesia. *Bulletin of Volcanology, 71*, 953–959.

Chow, V. T. (1959). *Open – channel hydraulics.* McGill Hill.

Coussot, P. (1994). Steady, laminar, flow of concentrated mud suspension in open channel. *J. Hydraul. Res., 32*, 535–559.

Coussot, P., & Meunier, M. (1996). Recognition, classification and mechanical description of debris flows. *Earth – Sciences Reviews, 40*(3–4), 209–227.

Coussot, P., & Piau, J. M. (1994). Rheology of highly concentrated suspensions of coarse particles. *Cah. Rhéol. (J. French Rheol. Group), XIII*, 266–277.

Daido, A. (1971). On the occurrence of mud-debris flow. *Disaster Prevention Res. Inst. Bull., 21*, 126–169.

DHI. (2009). *MIKE11: A modelling system for Rivers and Channels, Users Guide.* DHI.

Dunning, S., Large, A. R., Russell, A. J., Roberts, M. J., Duller, R., Woodward, J., Mériaux, A. S., Tweed, F. S., and Lim, M. (2013). The role of multiple glacier outburst floods in proglacial landscape evolution: the 2010 Eyjafjallajökull eruption Iceland. *Geology, 41*(10), 1123–1126.

Elíasson, J., Kjaran, S. P., Holm, S., Gudmundsson, M. T., & Larsen, G. (2007). Large hazardous floods as translatory waves. *Environmental Modelling & Software, 22*, 1392–1399.

Gerhart, P. M., Gross, R. J., & Hochstein, J. I. (1993). *Fundamentals of Fluid Mechanics* (2nd ed.). Addison-Wesley.

Gíslason, E., & Jóhannesson, T. (2007). *Calibration of the samos AT 2D avalanche model for large Icelandic dry-snow avalanches.* Reykjavík: Icelandic Meteorological Office.

Gíslason, M. B. (2012). *Straumfræðileg hermun jökulhlaups niður suðurhlíðar Eyjafjallajökuls í apríl 2010: ákvörðun Manningsstuðla (Hydraulic modelling of April 2010 glacial outburst on the southern slopes of Eyja-fjallajökull: choice of Manning coefficient).* Reykjavík: University of Iceland.

Gudmundsson, M. T., Högnadóttir, Þ., & Magnússon, E. (2015). Öræfajökull: Eruption melting scenarios. In E. Pagneux, M. T. Gudmundsson, S. Karlsdóttir, & M. J. Roberts (Eds.), *Volcanogenic floods in Iceland: An assessment of hazards and risks at Öræfajökull and on the Markarfljót outwash plain* (pp. 45–72). Reykjavík: IMO, IES-UI, NCIP-DCPEM.

Hákonardóttir, K. M., Jóhannesson, T., & Sampl, P. (2005). Líkanreikningar á jökulhlaupum niður suðurhliðar Eyjafjallajökuls (Hydraulic simulations of glacial outbursts on the southern slopes of Eyjafjallajökull). In M. T. Guðmundsson, & Á. G. Gylfason (Eds.), *Hættumat vegna eldgosa og hlaupa frá vestanverðum Mýrdalsjökli og Eyjafjallajökli (Hazard assessment of volcanic eruptions and glacial outbursts for Eyja-fjallajökull and the western outwash plain of Mýrdalsjökull)* (pp. 181–196). Reykjavík: Ríkislögreglustjórinn, Háskólaútgáfan.

Herschel, W. H., & Bulkley, R. (1926). Über die viskosität und Elastizität von Solen. *Am. Soc. Test. Mater., 26*, 621–633.

Hsü, K. (1975). Catastrophic debris streams (Sturzstroms) generated by Rockfalls. *GSA Bulletin, 86*(1), 129–140. doi:10.1130/0016-7606

Hubbard, B. E., Sheridan, M. F., Carrasco-Núñez, G., Díaz-Castellón, R., & Rodríguez, S. R. (2007). Comparative lahar hazard mapping at Volcan Citlaltépetl, Mexico using SRTM, ASTER and DTED-1 digital topographic data. *Journal of Volcanology and Geothermal Research, 160*, 99–124.

Iverson, R. M., Schilling, S. P., & Vallance, J. W. (1998). Objective delineation of lahar-inundation hazard zones. *Geological Society of America Bulletin, 110*, 972–984.

Johnson, A. M. (1970). *Physical Processes in Geology.* San Francisco: Freeman, Cooper.

Jóhannesson, T., Björnsson, H., Magnússon, E., Guðmundsson, S., Pálsson, F., Sigurðsson, O., Thorsteinsson, T., and Berthier, E. (2013). Ice-volumes changes, bias estimation of mass-balance measurements and changes in subglacial lakes derived by lidar mapping of the surface of Icelandic glaciers. *Annals of Glaciology, 54*(63), 63–74.

Jóhannesson, T., Björnsson, H., Pálsson, F., Sigurðsson, O., & Thorsteinsson, T. (2011). LiDAR mapping of the Snæfellsjökull ice cap, western Iceland. *Jökull, 61*, 19–32.

Leyrit, H., & Montenat, C. (2000). *Volcaniclastic Rocks from magmas to sediments.* Gordon and Breach Science Publishers.

Locat, J., & Demers, D. (1988). Viscosity, yield stress, remolded strength, and liquidity index relationships for sensitive clays. *Can. Geotech. J., 25*, 799–806.

Lun, C. K., Savage, S. B., Jeffrey, D. J., & Cherpurniy, N. (1984). Kinetic theories for granular flow: inelastic particles in Couette flow and slightly inelastic particles in a general flowfield. *J. Fluid Mech., 140*, 223–256.

Magirl, C. S., Griffiths, P. G., & Webb, R. H. (2010). Analyzing debris flows with the statistically calibrated empirical model LAHARZ in south–eastern Arizona, USA. *Geomorphology, 119*(1-2), 111–124.

Magnússon, E., Gudmundsson, M. T., Sigurdsson, G., Roberts, M. J., Höskuldsson, F., & Oddsson, B. (2012a). Ice-volcano interactions during the 2010 Eyjafjallajökull eruption, as revealed by airborne radar. *J. Geophys. Res., 117, B07405*. doi:10.1029/2012JB009250

Magnússon, E., Pálsson, F., Björnsson, H., & Gudmundsson, S. (2012b). Removing the ice cap of Oraefajokull central volcano, SE-Iceland: Mapping and interpretation of bedrock topography, ice volumes, subglacial troughs and implications for hazards assessments. *Jökull, 62*, 131–150.

Major, J. J., & Pierson, T. C. (1992). Debris flow rheology: Experimental analysis of fine-grained slurries. *Water Resour. Res., 28*, 841–857.

Malin, M., & Sheridan, M. (1982). Computer-Assisted Mapping of Pyroclastic Surges. *Science, 217*(4560), 637–640.

Michaels, A. S., & Bolger, J. C. (1962). The plastic flow behavior of floculated kaolin suspensions. *Ind. Eng. Chem. Fundam., 1*, 153–162.

Muñoz-Salinas, E., Castillo-Rodriguez, M., Manea, V., Manea, M., & Palacios, D. (2010). On the geochronological method versus flow simulation software application for Lahar risk mapping: A case study of Popocatepetl volcano. *Geografiska Annaler, Series a – Physical Geography, 92*(A), 311–328.

Muñoz-Salinas, E., Castillo-Rodríguez, M., Manea, V., Manea, M., & Palacios, D. (2009). Lahar flow simulations using LAHARZ program: Application for the Popocatépetl volcano, Mexico. *Journal of Volcanology and Geothermal Research, 182*(1-2), 13–22.

Nguyen, Q. D., & Boger, D. V. (1983). Yield stress measurement for concentrated suspensions. *J. Rheol., 27*, 321–349.

Nye, J. F. (1976). Water flow in glaciers: Jökulhlaups, tunnels and veins. *Journal of Glaciology, 17*(76), 181–207.

Pagneux, E. (2015a). Öræfi district and Markarfljót outwash plain: Spatio-temporal patterns in population exposure to volcanogenic floods. In E. Pagneux, M. T. Gudmundsson, S. Karlsdóttir, & M. J. Roberts (Eds.), *Volcanogenic floods in Iceland: An assessment of hazards and risks at Öræfajökull and on the Markarfljót outwash plain* (pp. 123–140). Reykjavík: IMO, IES-UI, NCIP-DCPEM.

Pagneux, E. (2015b). Öræfajökull: Evacuation time modelling of areas prone to volcanogenic floods. In E. Pagneux, M. T. Gudmundsson, S. Karlsdóttir, & M. J. Roberts (Eds.), *Volcanogenic floods in Iceland: An exploratory assessment for Öræfajökull and the Markarfljót outwash plain* (pp. 141–164). Reykjavík: IMO, IES-UI, NCIP-DCPEM.

Pagneux, E., & Roberts, M. J. (2015). Öræfi district and Markarfljót outwash plain: Rating of flood hazards. In E. Pagneux, M. T. Gudmundsson, S. Karlsdóttir, & M. J. Roberts (Eds.), *Volcanogenic floods in Iceland: An assessment of hazards and risks at Öræfajökull and on the Markarfljót outwash plain* (pp. 103–124). Reykjavík: IMO, IES-UI, NCIP-DCPEM.

Pierson, T. C. (1998). An empirical method for estimating travel times for wet volcanic mass flows. *Bull Volcanol, 60*, 98–109.

Roberts, M. J. (2002). *Controls on supraglacial outlet development during glacial outburst floods.* Unpublished PhD thesis.

Roberts, M. J. (2005). Jökulhlaups: a reassessment of floodwater flow through glaciers. *Reviews of Geophysics, 43*, 1–21.

Roberts, M. J., & Gudmundsson, M. T. (2015). Öræfajökull Volcano: Geology and historical floods. In E. Pagneux, M. T. Gudmundsson, S. Karlsdóttir, & M. J. Roberts (Eds.), *Volcanogenic floods in Iceland: An assessment of hazards and risks at Öræfajökull and on the Markarfljót outwash plain* (pp. 17–44). Reykjavík: IMO, IES-UI, NCIP-DCPEM.

Russell, A. J., Tweed, F., Roberts, M. J., Harris, T. D., Gudmundsson, M. T., Knudsen, O., & Marren, P. M. (2010). An unusual jökulhlaup resulting from subglacial volcanism, Sólheimajökull, Iceland. *Quaternary Science Review*, 1363–1381.

Sampl, P., & Granig, M. (2009). Avalanche simulation with SAMOS-AT. *International Snow Science Workshop Proceedings*, (pp. 519–523). Davos, GR, Switzerland.

Sampl, P., & Zwinger, T. (2004). Avalanche simulation with SAMOS. *Annals of Glaciology, 38*, 393–398.

Savage, S. B. (1984). The mechanics of rapid granular flows. *Adv. Appl. Mech., 24*, 289–366.

Schilling, S. P. (1998). *LAHARZ: GIS programs for automated mapping of Lahar – inundation hazard zones.* Vancouver: U.S. Geological Survey Information Services.

Snorrason, Á., Einarsson, B., Pagneux, E., Hardardóttir, J., Roberts, M., Sigurðsson, O., Thórarinsson, Ó., Crochet, P., Jóhannesson, T., and Thorsteinsson, T. (2012). Floods in Iceland. In Z. W. Kundzewicz (Ed.), *Changes in flood risk in Europe* (pp. 257–276). IAHS Special Publication 10.

Stevens, N. F., Manville, V., & Heron, D. W. (2003). The sensitivity of a volcanic flow model to digital elevation model accuracy: experiments with digitised map contours and interferometric SAR at Ruapehu and Taranaki volcanoes, New Zealand. *Journal of Volcanology and Geothermal Research, 119*(1–4), 89–105.

Takahashi, T. (1978). Mechanical characteristics of debris flow. *J. Hydraul. Div., 104*, 1153–1169.

Thorarinsson, S. (1958). The Öræfajökull eruption of 1362. *Acta Naturalia Islandica, 2*(4), 100.

Tómasson, H. (1996). The Jökulhlaup from Katla in 1918. *Annals of Glaciology, 22*, 249–254.

Wang, Z., Larsen, P., & Xiang, W. (1994). Rheological properties of sediment suspensions and their implications. *J. Hydraul. Res., 32*, 560–580.

Waythomas, C. F., Pierson, T. C., Major, J. J., & Scott, W. E. (2013). Voluminous ice-rich and water rich lahars generated during the 2009 eruption of Redoubt Volcano, Alaska. *Journal Volc. Geoth. Res., 259*, 389-413.

Zwinger, T., Kluwick, A., & Sampl, P. (2003). Simulation of Dry-Snow Avalanche Flow over Natural Terrain. In K. Hutter, & N. Kirchner (Eds.), *Dynamic Response of Granular and Porous Materials under Large and Catastrophic Deformations* (Vol. 11, pp. 161-194). Heidelberg: Springer.